Crust and Upper Mantle Structure Beneath the Eastern United States

Chengping Chai[1,1], Charles Ammon[2,2], Monica Maceira[3,3], and Herrmann B. Robert[4,4]

[1]Oak Ridge National Laboratory
[2]Pennsylvania State University
[3]Oak Ridge National Laboratory (DOE)
[4]Saint Louis U.

November 30, 2022

Abstract

The Eastern United States has a complex geological history and hosts several seismic active regions. We investigate the subsurface structure beneath the broader eastern United States. To produce reliable images of the subsurface, we simultaneously invert smoothed P-wave receiver functions, Rayleigh-wave phase and group velocity measurements, and Bouguer gravity observations for the 3D shear wave speed. Using surface-wave observations (3-250 s) and spatially smoothed receiver functions, our velocity models are robust, reliable, and rich in detail. The shear-wave velocity models fit all three types of observations well. The resulting velocity model for the eastern U.S. shows thinner crust beneath New England, the east coast, and the Mississippi Embayment. A relatively thicker crust was found beneath the stable North America craton. A relatively slower upper mantle was imaged beneath New England, the east coast, and western Mississippi Embayment. A comparison of crust thickness derived from our model against four recent published models shows first-order consistency. A relatively small upper mantle low-speed region correlates with a published P-waves analysis that has associated the anomaly with a 75 Ma kimberlite volcanic site in Kentucky. We also explored the relationship between the subsurface structure and seismicity in the eastern U.S. We found earthquakes often locate near regions with seismic velocity variations, but not universally. Not all regions of significant subsurface wave speed changes are loci of seismicity. A weak correlation between upper mantle shear velocity and earthquake focal mechanism has been observed.

Crust and Upper Mantle Structure Beneath the Eastern United States

Chengping Chai[1], Charles J. Ammon[2], Monica Maceira[1], Robert Herrmann[3]

[1]Oak Ridge National Laboratory, Oak Ridge, Tennessee, U.S.A.

[2]Department of Geosciences, Pennsylvania State University, University Park, Pennsylvania, U.S.A.

[3]Department of Earth and Atmospheric Sciences, Saint Louis University, St. Louis, Missouri, U.S.A.

Corresponding author: Chengping Chai (chaic@ornl.gov)

Key Points:

- Inverting smoothed receiver functions, surface-wave dispersion and gravity for a 3D shear wave velocity model for the eastern US
- Our velocity model is broadly consistent with published results for the region
- Earthquakes often but not universally locate near areas with seismic speed variation, but not all velocity changes are loci of seismicity

This manuscript has been authored in part by UT-Battelle, LLC, under contract DE-AC05-00OR22725 with the US Department of Energy (DOE). The US government retains and the publisher, by accepting the article for publication, acknowledges that the US government retains a nonexclusive, paid-up, irrevocable, worldwide license to publish or reproduce the published form of this manuscript, or allow others to do so, for US government purposes. DOE will provide public access to these results of federally sponsored research in accordance with the DOE Public Access Plan (http://energy.gov/downloads/doe-public-access-plan).

Abstract

The Eastern United States has a complex geological history and hosts several seismic active regions. We investigate the subsurface structure beneath the broader eastern United States. To produce reliable images of the subsurface, we simultaneously invert smoothed P-wave receiver functions, Rayleigh-wave phase and group velocity measurements, and Bouguer gravity observations for the 3D shear wave speed. Using surface-wave observations (3-250 s) and spatially smoothed receiver functions, our velocity models are robust, reliable, and rich in detail. The shear-wave velocity models fit all three types of observations well. The resulting velocity model for the eastern U.S. shows thinner crust beneath New England, the east coast, and the Mississippi Embayment. A relatively thicker crust was found beneath the stable North America craton. A relatively slower upper mantle was imaged beneath New England, the east coast, and western Mississippi Embayment. A comparison of crust thickness derived from our model against four recent published models shows first-order consistency. A relatively small upper mantle low-speed region correlates with a published P-waves analysis that has associated the anomaly with a 75 Ma kimberlite volcanic site in Kentucky. We also explored the relationship between the subsurface structure and seismicity in the eastern U.S. We found earthquakes often locate near regions with seismic velocity variations, but not universally. Not all regions of significant subsurface wave speed changes are loci of seismicity. A weak correlation between upper mantle shear velocity and earthquake focal mechanism has been observed.

Plain Language Summary

The Eastern United States experienced a complex series of geological activities. Earthquakes in the Eastern United States have been recorded at several localized regions. A detailed subsurface structure can help us recover the geological history and studying earthquakes. We use multiple types of geophysical observations to reliably image the subsurface. Our images of the subsurface confirmed many findings from previous studies. The crust is thinner beneath New England, the east coast, and the south-central United States. The interior of North America has a thicker crust. The upper mantle seismic speed is shower beneath New England, the east coast, and the western portion of the south-central United States. A smaller region of slower upper mantle speed in Kentucky agrees with a published study, which linked the slower speed with a 75 Ma volcanic site. We compared images of subsurface against earthquake locations. Earthquakes often locate near regions with lateral subsurface structure changes. Lateral subsurface structure changes do not always collocate with earthquakes. The type (faulting) of earthquakes weakly correlates with the upper mantle seismic speed.

1 Introduction

The eastern United States (EUS) has a long and complex geological history that includes at least two episodes of continental collision and breakup. The eastern part of North America grew from the continent's Archean core through arc and continental collisions in the Early-Middle Proterozoic (e.g., Whitmeyer, 2007). The resulting supercontinent Rodina broke up during the opening of the Iapetus Ocean in the Late Proterozoic (Hynes & Rivers, 2010). Renewed plate convergence and episodic terrane accretion formed the supercontinent Pangea during the Paleozoic and the early Mesozoic (e.g., Hatcher, 2010; Whitmeyer, 2007). The opening of the Atlantic Ocean started in the Triassic-Jurassic (Hames et al., 2000). The east coast became a passive margin around 180 Ma (Faill, 1998). Several stages of rifting modified the passive margin (e.g., Whitmeyer, 2007). Except for first-order observations of a relatively fast upper mantle, the relationship between the geological history and subsurface structure is still not well known.

Though the EUS is naturally less seismically active than the western U.S., several intraplate seismic zones (see Figure 1) including the New Madrid seismic zone (NMSZ), the Wabash Valley seismic zone (WVSZ), the South Carolina seismic zone, the Central Virginia seismic zone, and the West Quebec seismic zone (WQSZ) show localized seismic activity in the east coast. Three great-to-major earthquakes (Magnitude 7-to-8) struck the NMSZ in 1811-1812 and caused severe damage (Hough et al., 2000; Johnston, 1996). Paleoseismic studies suggest that at least two large earthquakes occurred thousands of years prior to 1800 (Tuttle, 2002). Past destructive earthquakes and slow deformation (Newman, 1999) provoke debate over the seismic hazard assessment (Stein, 2007). The mechanism of stress concentration that is proposed to have caused these large events is unsolved. Some geodynamic models predicted a stress concentration in the seismogenic zone (e.g., Levandowski et al., 2016; Pollitz, 2001). However, the assumed structural models differ significantly due to poor images of the subsurface, especially in the crust. Detailed structure images beneath the EUS are required to answer outstanding questions such as what factors control the occurrence of intraplate earthquakes.

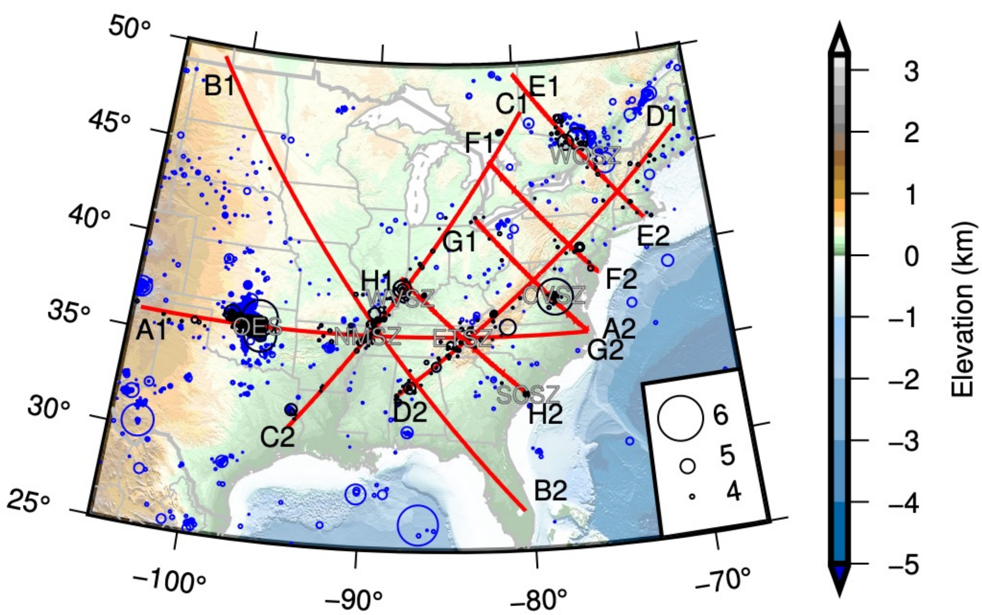

Figure 1. Seismicity (black and blue circles, magnitude 3 and larger prior May 2021 from the USGS catalog) and cross-section locations (red lines). Black cirlces represent earthquakes that are shown in cross-sections. Blue circles are earthquakes that are located 100 km away from any cross-sections. The size of circles is proportion to magnitude. Abbreviations: CVSZ – Central Virginia Seismic Zone; ETSZ – Eastern Tennessee Seismic Zone; NMSZ – New Madrid Seismic Zone; OES – Oklahoma Earthquake Swarm; SCSZ – South Carolina Seismic Zone; WQSZ – West Quebec Seismic Zone; WVSZ – Wabash Valley Seismic Zone. (For interpretation of the references to color in this figure, the reader is referred to the web version of this article.)

The deployment of EarthScope USArray Transportable Array (TA) provided unprecedented station coverage in the EUS for more than 10 years. The TA has crept continuously across the U.S. and collected seismic observations at more than 2000 unique locations. With a nearly uniform station spacing (~70 km) and high-quality sensors, the array was designed to improve our understanding of subsurface structure and have led to many seismic velocity models for the lithosphere structure of the EUS and surround regions (e.g., Biryol et al., 2016; Bollmann et al., 2019; Dong & Menke, 2017; Golos et al., 2018; Menke et al., 2018; B. Savage et al., 2017; Brian Savage, 2021; Wagner et al., 2018; B. B. Yang et al., 2014). To better utilize the improved data coverage and compare the subsurface structure across a broad region, we investigate the seismic velocity variations beneath the EUS with a model parameterization that is suitable for TA stations.

Even with dense seismic networks, tightly constraining subsurface 3D geologic variations is a challenge. But the seismological community has worked for decades with less data to extract information valuable enough to steadily advance our understanding of the lithosphere. P-wave receiver functions processed from teleseismic P-waves provide us a way to repeatedly sample subsurface structure beneath seismic stations as source-side effects are removed by deconvolution (e.g., Langston, 1979). To extract detailed subsurface structural parameters from receiver functions, an inversion is often used to estimate model parameters from receiver function observations. The inversion of receiver functions is non-unique (e.g., Ammon et al., 1990), but incorporating complementary observations has shown to ease the non-unique problem and improve the sensitivity (e.g., Chai et al., 2015; Chong et al., 2016; Julià et al., 2000, 2003; Özalaybey et al., 1997; Sun et al., 2014). The construction of 3D models adds additional complexity. Different data sets may average 3D heterogeneity differently, making one-dimensional models that fit all the data difficult to construct. For example, 3D scattering in receiver functions can introduce hard-to-identify high-wavenumber artifacts during an inversion. An often used and generally successful approach to reduce these effects is to target smooth earth models that represent averages of the true structure. We used the receiver function smoothing/interpolation technique (Chai et al., 2015) to reduce the scattering noise in the data prior to the inversion to avoid mapping noise into artifacts. Simultaneous inversion using smoothed receiver functions has produced reliable images of subsurface seismic velocity variations (Chai et al., 2015).

We simultaneously inverted smoothed/interpolated P-wave receiver functions, Rayleigh-wave phase and group velocity measurements, and Bouguer gravity observations for subsurface structure beneath the EUS using linearized uniform-cell-based 3D inversions. Compared with recent studies (e.g., Porter et al., 2016; Schmandt et al., 2015; Shen & Ritzwoller, 2016), we used a wider period range for surface-wave dispersion observations, included longer receiver function signals, and reduced scattering noise in receiver functions through spatially smoothing. We describe the procedures used to process each observation type in the next section. Details of the receiver function smoothing/interpolation technique are discussed in the following section and are followed with a description of the theory and processes for the simultaneous inversion. The fits to each type of observations are illustrated in a separate section to show an important component of the quality control applied to our results. We end with a discussion on the resulting 3D shear-wave velocity models that compares our results with recently published models and an investigation of the relationship between seismicity and subsurface material variations.

2 Data

We used three types of geophysical observations to image the subsurface structure including P-wave receiver functions, Rayleigh-wave dispersion measurements, and Bouguer gravity observations. The receiver functions were computed using observations from about 1700 seismic stations operated within the broad EUS (Figure S1).

2.1 Receiver function observations

P-wave receiver functions were processed using teleseismic waveforms recorded at TA, and many other seismic networks (a complete list of networks can be found in Table S1). Seismic events (around 3,700) with body-wave magnitude m_b larger than 5.7 during station operation times (prior June 2015) and at epicentral distances from 30 to 100˚ (see Figure S2) were selected to avoid P-waveform interference with upper mantle triplications and the core shadow zone. We downloaded three-component P-waveforms along with metadata for these events from the Data Management Center of Incorporated Research Institutions for Seismology (IRIS DMC). The seismograms were rotated to the radial-transverse-vertical system from the original north-east-vertical recording coordinates. P-wave receiver functions (Langston, 1979) were obtained by deconvolving the vertical component from the radial and transverse components using the time domain iterative deconvolution algorithm (Ligorría & Ammon, 1999). Gaussian filters (Ammon, 1991) were used in the deconvolution process to limit the bandwidth of the receiver functions and preserve absolute amplitudes of receiver functions. Specifically, we computed receiver functions with a Gaussian filter of 1.0 and 2.5 that correspond roughly to pulse widths of 1.67 and 0.67 s at half the maximum, respectively.

Similar to receiver functions obtained for the western U.S region (e.g., Chai et al., 2015), many receiver functions processed from even high-quality stations are quite noisy. In order to exclude noisy outliers, we used three programmable waveform selection criteria. Other waveform selection criteria have been used by previous studies (e.g., Yang et al., 2016), but visual examinations of our receiver function waveforms confirm that these three criteria are sufficient to remove problematic receiver functions from the data. First, receiver functions with signal-to-noise ratios (measured using a 170 s time window that ends 10 s earlier than the expected P arrival time as noise and a 130 s time window immediately after as signal) less than 10 were discarded. Second, since the deconvolution can be unstable, we reject receiver functions with convolution fit less than 85%; the convolution fit is computed as a signal power ratio between the radial component and a convolved signal of receiver function and the vertical component. Even with these relatively strict criteria, occasionally, some problematic receiver functions (e.g. unusual large amplitude, wrong polarity, low-frequency noise) could pass through and influence our observations. To identify these signals, we computed the signal difference of each receiver function with respect to the single-station averaged waveform to further clean up our receiver function data set and excluded receiver functions with signal difference larger than 300% of the stacked waveform signal power. The distribution of receiver function signal differences follows the extreme value distribution for the EUS data set (Figure S3), which suggests a small portion of receiver functions is significantly different from the single-station averaged receiver functions. We obtained around 228,000 (38% of the raw receiver functions) acceptable receiver functions in total. The accepted receiver functions were then binned into three ray parameter bins (smaller than 0.05 s/km, larger than 0.07 s/km and in between) for both

Gaussian 1.0 and 2.5 receiver functions. Therefore, we have six receiver function waveforms at a station when data are abundant.

2.2 Surface-wave dispersion observations

We used both Rayleigh wave group and phase velocity observations in the simultaneous inversion. We avoid Love waves to minimize complexity that may arise from anisotropy. Our results are thus an approximation of the potentially anisotropic Earth. Surface-wave dispersion observations from two studies were blended to combine the short period dispersion values from Herrmann et al. (2021) and longer period dispersion observations from Ekström (2011). The short period dispersion observations were measured using both earthquake signals and ambient noise cross-correlations. The measured dispersion observations were localized to grid points through a surface wave tomography (e.g., Ekström, 2011; Herrmann et al., 2021). The short period dispersion model used a 1˚-by-1˚ grid with a node at the center of each grid cell. Only the dispersion data corresponding to cells with good ray path coverage (at least 50 km of ray path) were used. We adopted the following formula from Maceira & Ammon (2009) for a smooth blending of the dispersion curves.

$$s(T) = \cos^2\varphi\, s_2(T) + \sin^2\varphi\ s_1(T) \qquad (1)$$

in which

$$\varphi = \frac{\pi}{2}\frac{1+\tanh[\varepsilon(T-T_C)]}{2}$$

In the expressions above, $s(T)$ is the blended dispersion value (group or phase velocity). T is the period, $s_1(T)$ is a value from the long-period dispersion tomography (Ekström, 2011), and $s_2(T)$ is a value from the short-period dispersion tomography (Herrmann et al., 2021) at the same period. φ is a control parameter that is a function of T_c and ε. ε is set equal to 0.5. T_c is the period around which we want to switch from short- and long-period surface wave observations. Since the available period range varies from location to location (due to ray path coverage differences), we used a grid search to determine the best transitional period (T_c). We tried a range of T_c and computed the gradient of the resulting dispersion curves. In order to minimize artificial anomalies caused by the blending, the optimal T_c is the one with a minimum gradient (the smoothest dispersion curve). All blended dispersion curves were visually examined and minor adjustments were made as needed. Generally, a dispersion-curve transition period between 30-40 s was chosen. The blended dispersion data set spans from 3 s to 250 s in the best case. As an example, the blended dispersion curves are compared with recent dispersion models (Bensen et al., 2007; Ekström, 2011, 2014; Herrmann et al., 2021; Jin & Gaherty, 2015) in Figure S4. The blending of dispersion curves greatly extended the period range and are consistent with alternative recent dispersion models at most places.

2.3 Gravity observations

Gravity observations were extracted from a global Bouguer gravity model WGM2012 (Balmino et al., 2012). This Bouguer gravity data set was computed by spherical harmonic analysis using ETOPO1 topography-bathymetry data and gravity observations from the EGM2008 global gravity model (Pavlis et al., 2012). The lateral resolution of the gravity data is 5 arc minutes (~9 km), which is higher than what we can resolve with a 1˚-by-1˚ grid in our inversion. The Bouguer gravity observations are averaged within a 1˚-by-1˚ grid for the EUS to reduce gravity anomalies that are due to smaller-scale structure perturbations. Long wavenumber gravity signals are primarily caused by deep density changes. However, interpretation of deep gravity signals is nonunique and can be associated with density variations, plate flexure, and upper mantle dynamic effects. We wavenumber filtered the gravity observations with a box-car filter so that the remaining gravity signals are mainly sensitive to the shallow density structure (upper ~15 km). Initial gravity observations from WGM2012 and wavenumber filtered gravity values are compared in Figure S5. The filtered gravity image shows fewer small scale and large wave-number variations than the raw image as expected.

3 Receiver-function smoothing/interpolation

P-wave receiver functions and surface-wave dispersion observations have different spatial (lateral) sensitivity. Receiver functions are sensitive to sharp changes in vertical and lateral structure. In particular, large, complicated (and hopelessly aliased) variations near the surface often strongly influence P-wave receiver functions. Surface-wave dispersion observations are more sensitive to longer wavenumber variations in the structure. We smoothed the receiver-function wavefield spatially to reduce near-surface scattering effects and to better complement the surface-wave dispersion measurements. We have developed receiver function smoothing/interpolation to attack this issue by simplifying the receiver function wavefield (Chai et al., 2015). The smoothing/interpolation reduces the scattering noise on receiver function observations and isolates the spatially coherent components of the signals (see Figure 2 and Figure S6). Compared with the traditional single-station-averaged receiver functions, interpolated/smoothed receiver functions are more consistent laterally for different lag times.

A spatially smoothed receiver function is computed by averaging receiver functions recorded at adjacent stations with distance-dependent weights. Smoothing/interpolation also equalizes the lateral sensitivity of receiver functions and surface-wave dispersion measurements, which can reduce potential inconsistencies between surface-wave observations and body-wave receiver functions. Interpolation also provides us a way to approximate receiver functions at grid points where surface-wave observations are commonly estimated by tomography. This functionality is quite useful especially for 3D inversions using multiple types of observations. We can express the receiver function wavefield as $R(x,y,t)$, where x and y are spatial coordinates (e.g. latitude and longitude), and t is lag time after the direct P wave. Then, the interpolated receiver function wavefield is computed using the following formula repeatedly for all locations of interest (e.g. grid points)

$$R_i(x_i, y_i, t) = \frac{\sum_{j=1}^{n} \omega_j R_j(x_j, y_j, t)}{\sum_{j=1}^{n} \omega_j}$$

with

$$\omega_j = \begin{cases} 1 \ \ if\ r_{ij} < d_1 \\ \dfrac{r_{ij} - d_1}{d_1 - d_2} + 1 \ \ if\ \ d_1 < \ r_{ij} < d_2 \\ 0 \ \ if\ r_{ij} > d_2 \end{cases}$$

where r_{ij} is the distance between the point of interest (x_i, y_i) and station location (x_j, y_j), and n is total number of stations. d_1 and d_2 ($d_1 < d_2$) are two distance parameters that control the distance range for the stations included in the averaging and the weight (w_j) of the different stations. Receiver functions recorded at stations at distances less than or equal to d_1 are weighted as 1. Stations located at distances between d_1 and d_2 are weighted between 0 and 1 with the weight linearly decreased from 1 at distance d_1 to 0 at distance d_2. Chai et al. (2015) compared smoothed receiver functions computed using several pairs of distance parameters for different seismic network configurations in the western U.S. In our analysis, we choose a d_1 of 110 km and a d_2 of 160 km for the EUS to match the 1˚ grid used for surface-wave dispersion tomography. By spatially smoothing the receiver function wavefield, we sacrifice spatial resolution for simplicity and better average properties, but we may blur some geological transitions and boundaries. The resulting smoothed receiver functions are more complementary to the surface-wave dispersion data and comprise a data set more consistent with the other observations used in the joint inversion and with less near-surface scattering effects that can complicate the inverse models.

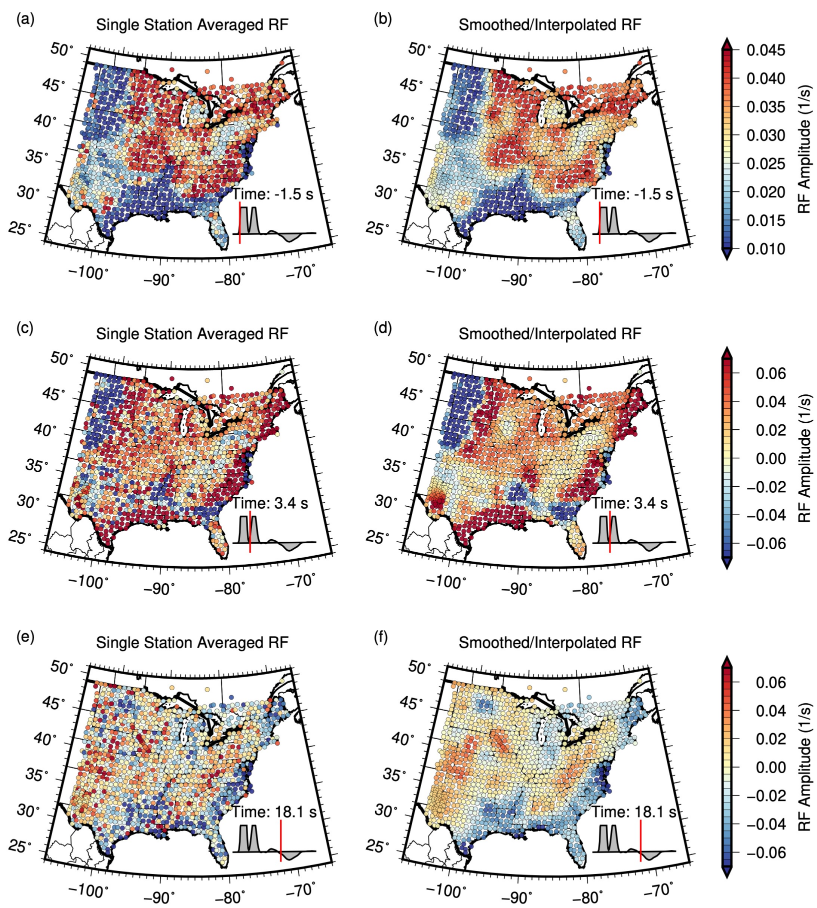

Figure 2. Time slice at time -1.5 s (a, b), 3.4 s (c, d) and 18.1 s (e, f) from receiver function wavefield in the EUS and adjacent Canada. Each circle represents a seismic station at which we have computed a stacked receiver function. The color indicates the amplitude of (a, c, e) the receiver function averaged at each station or (b, d, f) the smoothed/interpolated value of the receiver function wavefield. Inset shows the stack of all RFs (clipped to show details), and the red line shows the corresponding lag time of the time slice. See Movie S1 for all the time slices. (For interpretation of the references to color in this figure, the reader is referred to the web version of this article.)

4 Simultaneous inversion

To estimate the subsurface shear wave speeds beneath the EUS, we simultaneously inverted the smoothed/interpolated receiver function wavefield, Rayleigh wave group and phase velocities in the period range from 3 to 250 s, and wavenumber-filtered Bouguer gravity observations. The study region was divided into 950 1˚-by-1˚ size cells for the EUS so the best lateral resolution of our model is 110 km by 110 km. The resulting 3D grid was used for our simultaneous inversions in a hybrid 1D-3D manner. Receiver-function and surface-wave-dispersion calculations were performed with a 1D formalism for each cell across the region where observations are available. Gravity calculations were computed in 3D using rectangular prisms. The lateral dimension of the prisms is the same as the grid size whereas the vertical dimension varies from 1 km near the surface to 50 km in the mantle. A linearized discrete geophysical inversion developed from (Chai et al., 2015; Julià et al., 2000; Maceira & Ammon, 2009) was used with smoothness-based stabilization. A jumping strategy is used for regularization to allow constraints directly on model parameters, not changes in model parameters (e.g., Constable et al., 1987). The linearized inversion can be expressed as

$$\begin{pmatrix} \sqrt{\frac{p(T)}{\omega_s^2}}D_s \\ \sqrt{\frac{1}{\omega_r^2}}D_r \\ \sqrt{\frac{1}{\omega_g^2}}D_g \\ \eta\Delta \\ W \\ S \end{pmatrix} m_1 = \begin{pmatrix} \sqrt{\frac{p(T)}{\omega_s^2}}R_s \\ \sqrt{\frac{1}{\omega_r^2}}R_r \\ \sqrt{\frac{1}{\omega_g^2}}R_g \\ 0 \\ 0 \\ 0 \end{pmatrix} + \begin{pmatrix} \sqrt{\frac{p(T)}{\omega_s^2}}D_s \\ \sqrt{\frac{1}{\omega_r^2}}D_r \\ \sqrt{\frac{1}{\omega_g^2}}D_g \\ 0 \\ 0 \\ 0 \end{pmatrix} m_0 + \begin{pmatrix} 0 \\ 0 \\ 0 \\ 0 \\ W \\ 0 \end{pmatrix} m_a$$

where D_s, D_r and D_g are matrices containing the partial derivatives of the seismic shear velocity model corresponding to the dispersion, receiver function, and gravity estimates, respectively. m_0 is the 3D velocity model from previous iteration. m_a is the a priori velocity model. m_1 is the updated velocity model for the current iteration. R_s, R_r and R_g are the corresponding data residual vectors, and ω_s^2, ω_r^2 and ω_g^2 are global weights assigned to the three data sets. Those weights are defined in the same way as Julià et al. (2000) as $N\sigma_k^2$ where N is the number of data points for the specific data set and σ_k^2 is the kth data point variance. $p(T)$ was introduced by Maceira & Ammon (2009) to control the trade-off between fitting both gravity and surface-wave dispersion measurements. The matrix Δ applies vertical smoothing with a weight η to make the 1D velocity profiles vary smoothly - necessary when data constraints are not sufficient. W is a diagonal matrix to constrain the velocities from varying too far from the a priori values in m_a with associated weights. Lateral smoothing is added through the matrix S using the first differences between shear velocity values in adjacent grid cells. The lateral smoothing does not smooth across the ocean-continent boundary to allow a sharp change in material properties across this well-defined (for our cell size) feature. The inverse equation is solved using a Conjugate-Gradient LSQR solver for sparse linear equations (Paige & Saunders, 1982). The weights and smoothing parameters are determined by performing suites of inversions and comparing data misfits and model properties such as roughness. Interactive visualization tools were used to help the comparison of inversion results with different weighting parameters (Chai et al. 2018). The vertical smoothness constraints increase with depth to reflect a loss in data resolution and the increase in surface wavelengths sampling the greater depth in the model. Partial derivatives for surface wave dispersion were computed using finite-difference approximations. The simulation of surface-wave dispersion is based on algorithms from Saito (1988). The gravity derivatives were computed using the equations from Plouff (1976) and the chain rule. The inversion is performed to estimate shear-wave speed, which is related to P-wave speed by the V_p/V_s ratio, and to the density using formulas described in Maceira & Ammon (2009) and Chai et al. (2015). The V_p/V_s ratio was fixed throughout the inversion (inherited from the initial model).

The inversion for the EUS started with an initial model that was based on Crust Model 1.0 (Laske et al., 2013). Velocities below the crust were initialized with the AK135 velocity model (Kennett et al., 1995). Since flat-Earth codes were used to compute dispersion, the initial model was flattened using the formulas from Biswas (1972) with a slightly modified density transformation exponent (see the supplements of Chai et al., 2015 for details). Velocities and densities were unflattened prior to the gravity partial calculation and flattened after the gravity computation since the density-shear velocity relationship is based on laboratory measurements (corresponding to the spherical model).

Based on the results from hundreds of 3D inversions (multiple cells) and thousands of 1D inversions (single cell), it became clear that tuning the weights for each data set and constraints is necessary to produce good fits to the observations. We experimented with weight selection using numerous 1D inversions with observations selected from several samples in the overall data set. We searched for optimal ranges of weight parameters by randomly testing 1D inversion parameters, and examining the range of velocity models that resulted from the simulation. Within this suite of velocity models, some fit the data poorly. For many choices of the weights, the results were quite similar - those that fit the observations well often differed from the average model by less than 0.1 km/s. The tests suggest we can use data fits as a guide to select both the data and smoothness weights for the larger 3D inversions. To be sure that the resulting model fits the observations reasonably well, we used interactive visualization tools (Chai et al., 2018) to visually check data fits for all three types of observations.

The EUS results were obtained after eight total iterations of the 3D inversion (Figure S7). We began the inversion without gravity observations and modeled the seismic data for a total of four iterations. We then added the gravity observations for the final four iterations. The final EUS model has been unflattened for interpretation and easy comparison with published spherical Earth models.

5 Data fits

Fitting data is the most important quality control for our inversion. We discuss not only the overall data fit of the three types of observations we use but also the spatial distribution of data misfits. Fit to surface-wave dispersion and receiver functions is significantly improved in the first four iterations and are stable for the last four iterations (Figure S7). Gravity misfit was reduced greatly after one iteration. In general, our inverted model fits all three types of observations much better than the starting model. Figure 3 shows the receiver function and surface-wave dispersion misfit distributions of all cells for the initial and final models. In all cases, an improvement in fit is clear. We use a 95% threshold to quantify the overall misfit. The 95% misfit threshold represents the fractional misfit value equal to or larger than that found for 95% of the cells. The metric is used to eliminate the influence of the worst fitting 5% of the cells (which are often in the ocean, where data coverage is substantially more limited). As shown in

Figure 3, the 95% misfit threshold was improved from 15.5% (initial model) to 6.5% (inverted model) for group-velocity measurements, from 8% (initial model) to 2.5% (inverted model) for phase-velocity measurements, from 102% (initial model) to 33% (inverted model) for Gaussian 1.0 receiver functions, and from 132% (initial model) to 54% (inverted model) for Gaussian 2.5 receiver functions. The modest reduction in dispersion misfits reflects the relatively small range of speeds within the data. Any model with a roughly correct average dispersion value performs reasonably well with this metric. As expected, phase-velocity measurements are fit better than group-velocity measurements. Narrowband receiver functions were fit better than broadband receiver functions.

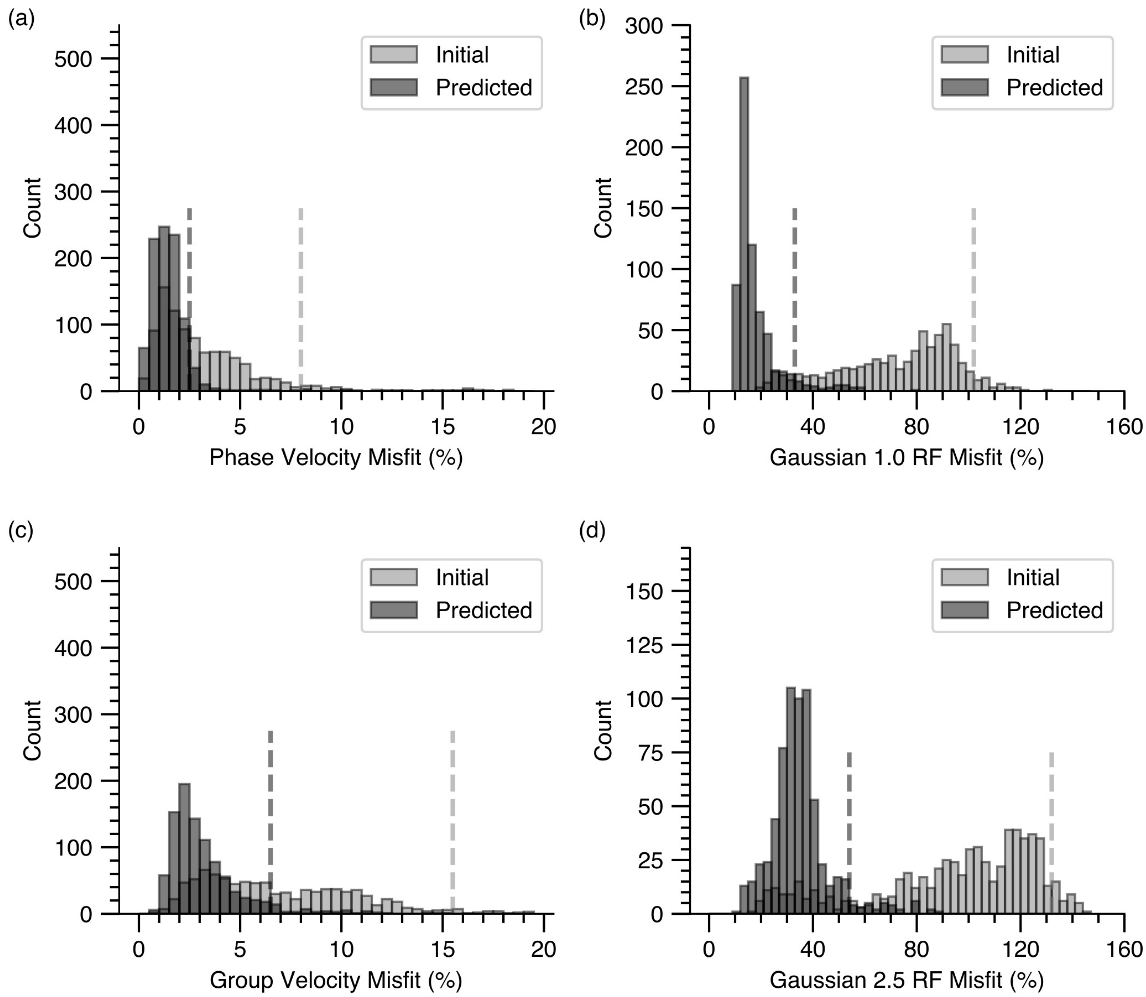

Figure 3. Comparison of misfit using the initial model (lighter color) and the inverted model (darker color) for (a) phase velocity, (b) Gaussian 1.0 receiver functions, (c) group velocity, and (d) Gaussian 2.5 receiver functions. Dashed lines show the misfit value that is larger than misfits for 95% of measurements. A root-mean-squared (RMS) misfit is normalized with the RMS of the corresponding observation.

5.1 Receiver function misfits

In Figure S8, we show the spatial distribution (at available grid points) of receiver function misfits for both the initial model and the inverted (final) model. Receiver function misfits computed from the initial model are quite large at most grid points. The misfit shown in the maps (Figure S8a and b) is the average of those corresponding to all available (up to six) receiver functions. For example, at the location corresponding to Figure S8c, the misfit (represented as the circle size in Figure S8a and b) is computed from six receiver functions (three ray parameter bins and two Gaussian widths). Comparing the observed and predicted receiver functions in Figure S8c, we found the converted phase and multiples arrive later in initial-model receiver functions. Receiver functions computed from the inverted model agree well with observations. At many grid points, the receiver functions computed with the initial model differ significantly from the observations, while the inverted model fit the obervations nicely (see Figure S8d for an example). Receiver function misfits corresponding to the inverted model are uniformly small with slightly larger values in Gulf of Mexico coastal regions and the Williston basin where thick sediments complicate receiver function waveforms. The relatively large misfits in the eastern Tennessee and western North Carolina may due to anisotropy or less-optimal V_p/V_s ratios.

5.2 Surface-wave dispersion misfits

The spatial distribution of surface-wave dispersion misfits (an average of group and phase speed misfits) is shown in Figure S9. Group and phase velocities computed from the initial model differ significantly from surface-wave dispersion observations for most model grid points as indicated by cells with large circles in Figure S9a. For example, we compared observed and simulated dispersion curves at a grid point located in northeast Mississippi in Figure S9c. Predicted dispersion curves based on the inverted model agree well with the observations while simulated group and phase velocities from the initial model are too small at most periods. Even for regions that the initial-model-derived surface-wave dispersion curves are similar to observations (see Figure S9d for an example), the inverted model predicts the surface-wave measurements better, especially at short periods (less than 20 s). As shown in Figure S9c, surface-wave dispersion misfits corresponding to the inverted model are much smaller than those from the initial model except for a few off-coast locations. Large misfits at these off-coast grid points (at the gulf coast of Florida and near northern NewJersey) are likely due to limited observations and a poor starting model.

5.3 Gravity misfits

Gravity observations are much fewer in number compared to receiver functions and surface-wave dispersion. For this reason, we use a smaller weight for gravity observations and include gravity data at a later stage of the inversion. The predicted gravity values agree with Bouguer gravity observations well (Figure S10). Since the gravity calculations are performed in 3D, we used a buffer zone (gray color filled regions in Figure S10) to avoid edge effects. In general, our goal with the gravity data is to fit the relatively high-wavenumber features that are likely associated with crustal density variations. The addition of gravity to the inversion does not introduce significant changes to the model. However, these changes are necessary to fit the gravity observations. Numerical tests showed that small changes of roughly 0.1 km/s to the upper

15 km account for an improved fit to the gravity. We only fit the first-order features in gravity observations to avoid overfitting.

6 Results

Representative shear-velocity depth slices are shown in Figure 4. Maps in Figure 4a-b are a plot of the average speed within the specified depth range. At shallow depth (0-5 km, Figure 4a), low velocities correlate well with major sedimentary basins and the coastal plains. Low velocity layers near the surface are thick along the coastal plains and within the basins of the Great Plains, compared with the Michigan, Illinois, and Appalachian basins. Average lower upper-crustal shear velocities are lower beneath the Mid-continent rift, which interrupts the relatively fast shallow crusts of Wisconsin and northern Minnesota and the Canadian Shield regions to the north and continues southward through southern Minnesota and Iowa. There is a hint (solid ellipse in Figure 4b) of a sharper transition along the northern (western) Mississippi Embayment (ME) boundary than along the east. Seismicity extends from the lower shear wave speeds into a region of more normal speeds. On average, the Appalachian region and the Midwest appear slightly faster than the region to the west that includes Wisconsin, Iowa, Nebraska, Kansas, and Oklahoma. The fast region in the northwest lies beneath the Williston Basin and is not well resolved, but the model, driven by dispersion measurements at these depths, suggests perhaps an unusually fast middle crust beneath the basin (Figure 4b). Two east-coast regions, the Carolinas and southern Virginia, and Maine appear slower than regions immediately west in the middle crust (Figure 4b).

Figure 4c is a map of the shear-velocity model at 37 km depth. This depth was chosen to provide first-order information on crustal thickness - in areas of thin crust, we see mantle-like speeds (dark blue colors, V_s larger than 4.4 km/s), while in many other areas, we simply see the lower crust. The map identifies the southern ME and coastal regions as regions of unusually thin crust. Regions of relatively fast deep crust are suggested in the eastern Dakotas, beneath Michigan, and parts of Canada and New England (see Figure 5 for crust thickness variations). We discuss specific estimates of crustal thickness later. Figure 4d is a map of the shear-wave model at a depth of 63 km, which provides a sample of the shear-wave speeds in the uppermost mantle. The range of velocity variation is about 6%. The image indicates a relatively slower upper mantle along the east coast from New England to South Carolina. A low velocity feature extends from the northern ME south to Louisiana and east Texas. The fastest speeds are to the north, into the Canadian Shield region.

Figure 5 includes a crustal thickness map along with example velocity profiles that were extracted from the model. Example velocity profiles at eight different locations (Figure 5a-d, f-i) show detailed velocity changes as a function of depth. To define crustal thickness, we measured the depth corresponding to P-wave velocity larger than 7.8 km/s (based on visual inspections of velocity profiles). Only a few cells failed to reach this speed before a depth of 53 km. The automatically measured crustal thicknesses are shown as dashed gray lines in Figure 5a-d,f-i, which match the crust-mantle transition well visually at all presented locations.

Our smoothing approach to receiver functions and reliance on surface-wave dispersion tomography to constrain the deeper features in the model increase the consequences of the assumption of sharp features such as the crust-mantle boundary in the initial model (Crust 1.0) on the location of the crust-mantle transition. However, as shown earlier, even when the model is good, slight adjustments are made to improve the alignment of the converted phases originating from the crust-mantle boundary region. Although we did not perform a rigorous analysis, our examination of the model suggests that when the constraints used to build Crust 1.0 were based on good nearby data, little adjustment in crustal thickness was needed by our inversion. In regions where we believe that Crust 1.0 relied heavily on interpolation, the inversion changes from our initial model were larger. Although adjustments are generally not large, typically 3 km, our model is almost systematically thinner than Crust 1.0 by a few kilometers (both models share the same V_p/V_s ratio).

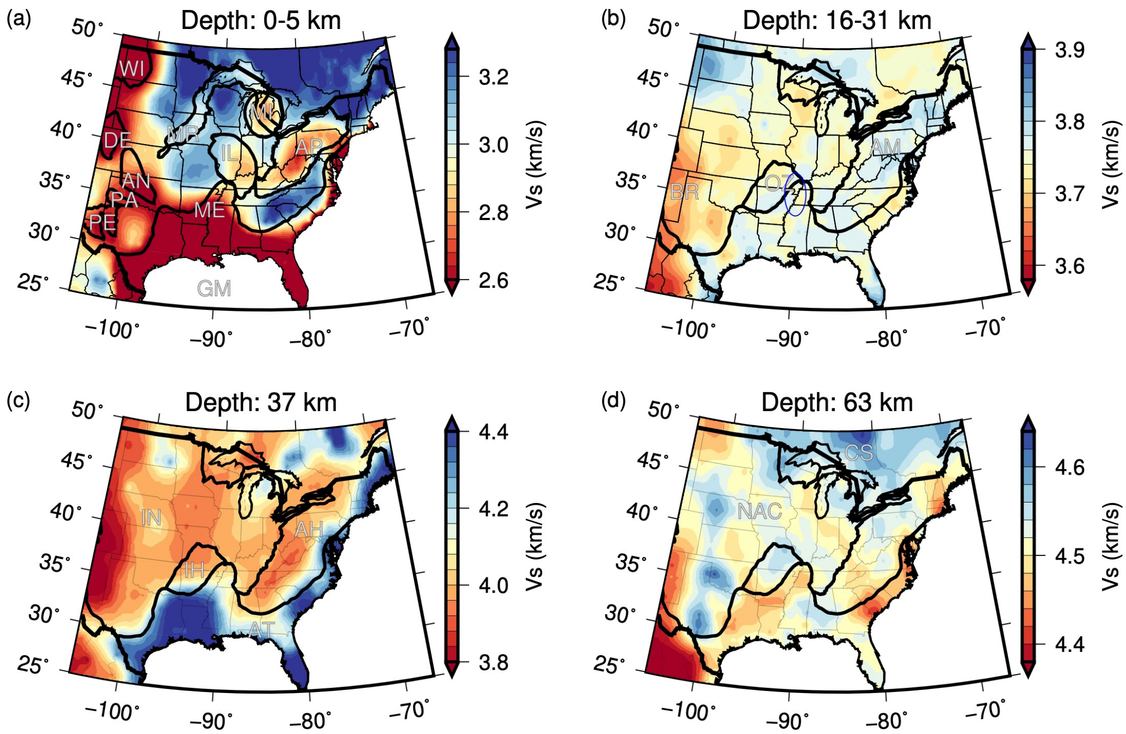

Figure 4. Shear-velocity maps showing depth range (a) 0-5 km, (b) 15-31 km, (c) 37 km, and (d) 63 km from the 3D model. Thick black lines in (a) indicate major sedimentary units. Thick black lines in (b), (c) and (d) show the physiographic boundaries. Thin black lines show state boundaries. Warm colors show relatively slower regions, cool colors indicate relatively faster regions. Although the colors are constant, the velocity range in each figure varies substantially. The anomalies at 0-5 km depth are primarily corresponding to sedimentary basins. The velocity changes at 15-31 km depth are related to lateral variations in mid-lower crust structure. Abbreviations: AH – Appalachian Highlands; AM – Appalachian Mountains; AN – Anadarko Basin; AP – Appalachian Basin; AT – Atlantic and Gulf Coastal Plains; BR – Basin and Range; CS – Canadian Shield; DE – Denver Basin; GM – Gulf of Mexico; IH – Interior Highlands; IL – Illinois Basin; IN – Interior Plains; ME – Mississippi Embayment; MI – Michigan Basin; MR – Midcontinent Rift; NAC – North America craton; OZ – Ozark Uplift; PA – Palo Duro Basin; PE – Permian Basin; WI – Williston Basin. (For interpretation of the references to color in this figure, the reader is referred to the web version of this article.)

Crustal thickness patterns for eastern North America are familiar. The crust is thinner near the coast and thicker landward. The average crustal thickness in the region is 43 km with a standard deviation of 5 km. Relatively thinner crust (< 43 km) is also imaged beneath eastern

North Dakota. The crust beneath the ME and into east Texas appears significantly thinner (< 35 km) than the continental interior. Thicker crust (> 43 km) is found beneath the Appalachian Mountains and the Great Plains. The depth of the crustal-mantle transition is less well constrained beneath thick sedimentary basins due to the dominance of basin reverberations in the receiver functions. One potential application of our model is to form the basis of a wavefield downward continuation and decomposition (Chai et al., 2017; Langston, 2011) to extract receiver function signals generated from the crust-mantle transition from teleseismic P-wave seismograms assuming the shallow structure is known. We leave that analysis for future efforts.

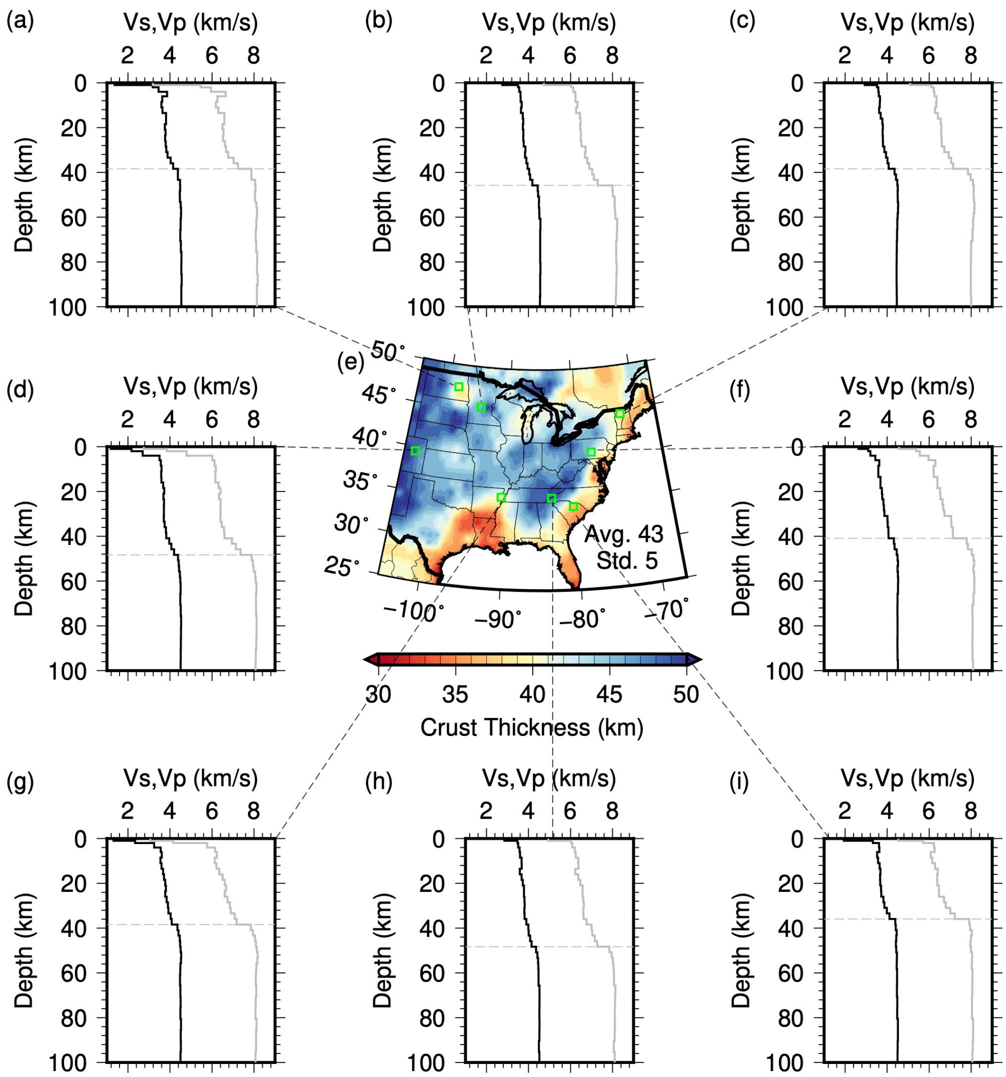

Figure 5. Crustal thickness map of (e) the EUS and (a-d, f-i) example velocity profiles at eight locations. Warm colors show relatively thinner crust, cool cools indicate relatively thicker crust. The average crustal thickness is 43 km with a standard deviation of 5 km. Green boxes on the map show the location of the corresponding velocity profile. In the profile plots (a-d, f-i), black lines represent shear-wave velocity while gray lines correspond to P-wave velocity. The dashed gray lines indicate the measured crustal thickness. (For interpretation of the references to color in this figure, the reader is referred to the web version of this article.)

We compared our crustal thickness measurements with several published models (Crotwell & Owens, 2005; Porter et al., 2016; Schmandt et al., 2015; Shen & Ritzwoller, 2016). The EARS (Crotwell & Owens, 2005) project measured crustal thickness from automatically computed P-wave receiver functions using H-k stacking method (Zhu & Kanamori, 2000) by assuming a constant velocity in the crust. The original results may suffer from scattering noise in receiver functions (e.g., Chai et al., 2015). We spatially smoothed the measured crustal thickness from EARS to show first-order features (see Figure S11). Comparing our crustal thickness map (Figure 5a) with four recently published models (Figure S12), we note that a thinner crust was imaged along the east coast and beneath the ME for all models. However, notable differences exist among these models. The average crustal thicknesses and the standard deviations from the Shen-2016 model (Shen & Ritzwoller, 2016), the Schmandt-2014 model (Schmandt et al., 2015), and our model are the same. The EARS model (Crotwell & Owens, 2005) may underestimate crustal thicknesses due to oversimplified model parameterization (constant-velocity crustal layer). The Porter-2015 model (Porter et al., 2016) used the EARS results to constrain crustal thickness and shared the same issue. The common conversion point (CCP) stacking procedure (Zhu, 2000) used for the Schmandt-2014 model reduced some scattering but had difficulty in challenging regions (sedimentary basins for example) where stacking energy is not focused. To a large degree, the Schmandt-2014 model, the Shen-2016 and our model are consistent. Small differences exsit between the Shen-2016 and our model (see Figure S13). The EARS model is certainly suitable for a starting model. We believe that our model is less contaminated by scattering in receiver functions and includes simultaneously-modeled constraints from Rayleigh waves (similar to the Shen-2016 model) and near-surface gravity.

Figure 6a and b are maps of the average crustal and upper-mantle shear-wave speed, respectively. The mean of the average crustal V_s velocity across the model continental grid points is 3.7 km/s (standard deviation 0.1 km/s). The corresponding mean crustal V_p velocity is 6.5 km/s (standard deviation 0.2 km/s, see Figure S14). These mean values agree reasonably well with the global compilation of Christensen & Mooney (1995). Relatively fast average crustal velocity is found beneath the stable North America craton. Regions of very slow average crustal shear-wave speeds are associated with thick sediments in the southern ME. The mean uppermost mantle shear-wave speed is the average of the upper 60 km of the mantle and it is 4.50 km/s (standard deviation 0.05 km/s). The average uppermost mantle P-wave speed in the study area is 8.1 km/s (standard deviation 0.1 km/s), which is also consistent with the global compilation (Christensen & Mooney, 1995) and regional surveys (Li et al., 2007). Note these P-wave speeds were derived from shear-wave speed using V_p/V_s ratios inherited from Crust 1.0. The uppermost mantle shear-wave velocity is slowest beneath New Mexico and the associated southern Basin and Range province. We imaged relatively slow average shear-wave speeds in the uppermost mantle beneath New England and the southeastern US, regions that may have interacted with Great Meteor (e.g., Eaton & Frederiksen, 2007) and Bermuda (e.g., Cox & Van Arsdale, 2002) hotspots respectively. Slow speeds along the east coast seem to follow the trend of eastern North America rift basins but extend further into northern New England than the surface expression of rifting. A slightly slower uppermost mantle is imaged beneath the western ME. Localized low average mantle speeds (dashed ellipses in Figure 6b) near the Kansas-Nebraska border and the Kentucky-Ohio border are situated near kimberlite volcanic site and may represent modified lithosphere associated with these volcanic structures. The relatively slow upper mantle weakly correlates with the region of thrust faulting along the eastern margin of the U.S. and within southeast Canada. The thrust faulting environment also correlates with the thin crust for much of the region, but not northern New York or southeastern Canada (Figure S15).

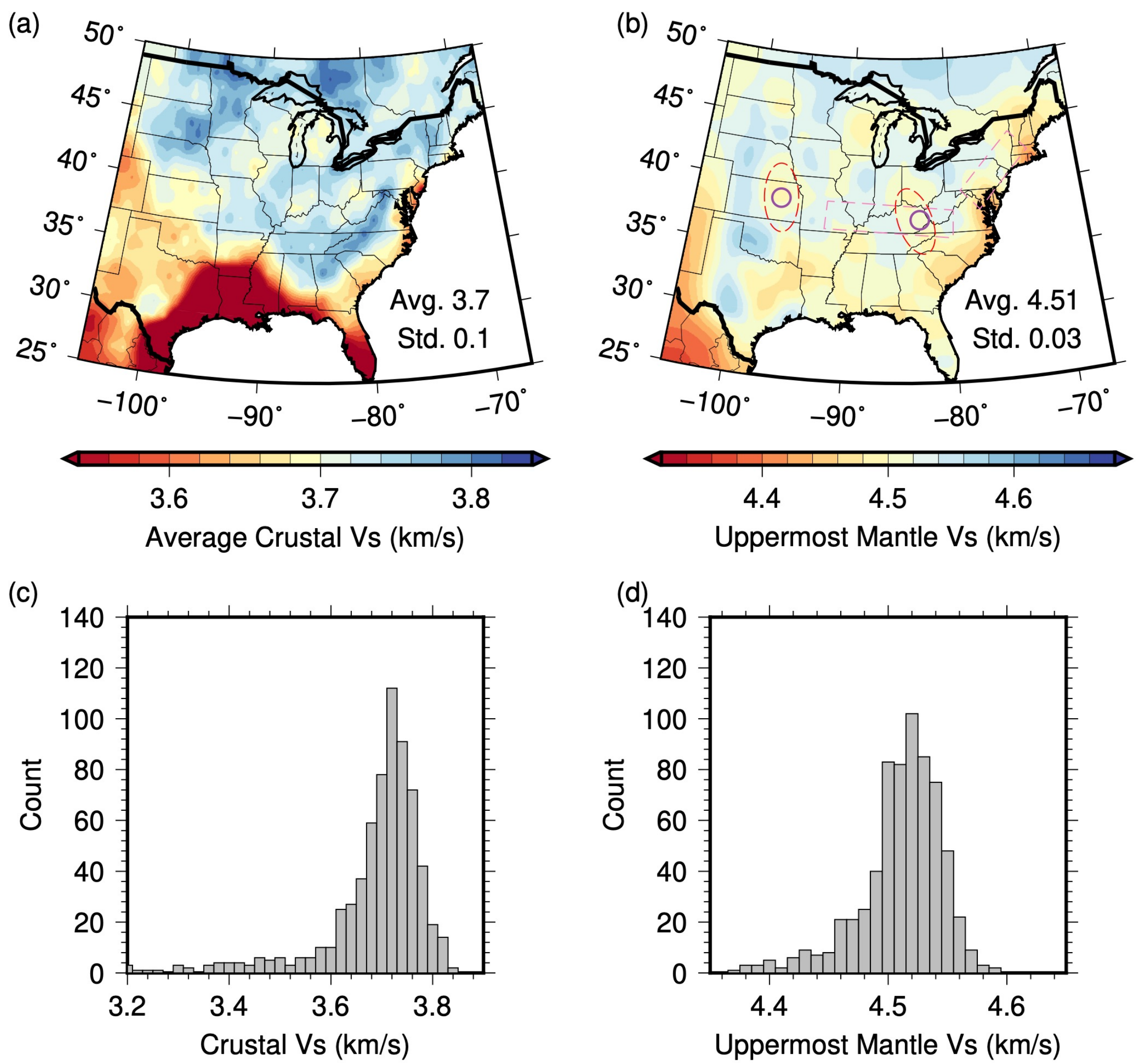

Figure 6. A summary of average crustal and mantle shear-wave velocity. (a) Average crustal shear-wave velocity map, (b) uppermost mantle shear-wave velocity map, and histograms of crustal V_s velocity (c) and uppermost mantle V_s velocity (d). The circles and rectangular boxes in (c) show locations of dated kimberlite intrusions and lithosphere anomalies from Chu et al. (2013), respectively. The mean (Avg.) of crustal V_s is 3.7 km/s with a standard derivation (Std.) of 0.1 km/s. The mean of uppermost mantle V_s is 4.51 km/s with a standard derivation of 0.03 km/s. The dashed ellipses show the locations of two slow velocity anomalies described in the text. (For interpretation of the references to color in this figure, the reader is referred to the web version of this article.)

We do not see any evidence for slower mantle resulting from lithospheric delamination and upwelling that is evident in geochemical observations (Mazza et al., 2014). Thus if lithospheric delamination and mantle upwelling occurred as the rocks suggest, the feature must be quite localized. The West Virginia-Virginia border overlies a relatively abrupt transition in crustal thickness. The crust is relatively flat towards the Appalachian interior from west to east but begins to thin near the area containing the kimberlite intrusions (see Figure 6b for the locations). More evidence for a significant change in lithospheric structure across the region is the difference in mid-crustal speed, which decreases by about 0.2-0.3 km/s from the Appalachians eastward (see Figure 4b). Although the transition is smoother, the upper mantle speed also decreases towards the east in the same region. The differences in structure suggest interesting geologic differences throughout the lithosphere from the Appalachians to central and eastern Virginia.

In Figure S16, we merged the EUS model with the published model in the western U.S. (Chai et al., 2015). The smooth transition from west to east indicates that our EUS model is compatible with the published western U.S. model. The anomalous upper mantle beneath the western ME, the east coast, and New England is modest compared with that beneath the Basin and Range province in the western U.S.

An automated cluster analysis (Chai et al., 2015) was used to group the 1-D shear velocity profiles into clusters of similar Earth structure. The spatial distribution of the clusters using shear velocities between the depth range of 5 and 200 km is shown in Figure S17. The clustered velocity models are shown in Figure S18. The crust is thinner beneath western ME, southern Basin and Range region, southern Interior Plains, and Atlantic Plain. A thicker crust was imaged beneath western Interior Plains, Appalachian Highlands, Interior Highlands, central Interior Plains. The southeastern Canadian Shield shows a slighter thinner crust. The upper mantle is faster beneath the stable North America craton. The seismicity in the region does not show a simple correlation to the subsurface seismic speed variation on the broad image in Figure S18. The clusters obtained with shear velocities between the depth range of 0 to 20 km is shown in Figure S19 and S20. To a certain extent, the distribution of clusters (Figure S19) can be used as a guide to the choice of a local 1D velocity model for initial earthquake location or moment tensor inversion. For instance, the same 1D velocity model may be used for the region specified by the same cluster. We use more detailed cross-sections to explore the relationship between the spatial distribution of earthquakes and subsurface structural variations.

7 Discussion

Large-scale regional lithospheric models contain many features that are often described in a list of short commentary related to geology. Many of the structural features that we observed have been pointed out in earlier studies (e.g., Chen Chen et al., 2016; Porter et al., 2016; Schmandt et al., 2015; Shen & Ritzwoller, 2016); we noted several of these in the Results section. One aspect not covered in other papers is the fact that a detailed crustal model provides an opportunity to explore the relationship(s) between seismicity and subsurface structure (if any exist). We use the cross-sections defined in Figure 1 to review the 3D model in details and to explore potential relationships between structure and seismicity. The cross-sections were chosen to cover most of the seismically active regions. Despite intensive studies, the cause of localized seismicity in the region remains poorly understood. Many ideas have been proposed to explain the intraplate seismicity of the EUS, such as stress concentration in regions of crustal weakness or changes in lithospheric structure (Grana & Richardson, 1996; Grollimund & D. Zoback, 2001; Kenner, 2000; Levandowski et al., 2016; Pollitz, 2001). Numerical models have shown that crustal deformation can be induced at shallow depth when a dense anomaly resides in the crust

(Levandowski et al., 2016; Pollitz, 2001; Zhan et al., 2016) above a relatively weak upper mantle. The depth and cause of a weak zone are still under debate (Chuanxu Chen et al., 2014; Pollitz & Mooney, 2014). Since seismicity in Oklahoma may be related to human activity, we skip that region (see Chai et al., 2021 for a detailed study of subsurface structure in that region). But note that ultimately, the Oklahoma activity is a result of the geologic structure associated with the hydrocarbon-rich basins in the area. The EUS model contains no significant features deep beneath the Oklahoma seismic activity. Two regions of particular interest are the northern ME and the Appalachian Mountains. We discussed some of the seismicity pattern and structure relationships for New Madrid in the Results section.

The cross-section A1-A2 (Figure 7) passes through seismically active regions in Oklahoma, the NMSZ, and the Eastern Tennessee Seismic Zone (ETSZ). The NMSZ is underlain by a relatively fast lower crust, which has been interpreted as a mafic intrusion (Catchings, 1999; Mooney et al., 1983). Reconstruction of the feature details is difficult with the coarse 100-km sampling, but the broader scale model shows the slower mantle in comparison with regions to the east and west. Numerical tests and Rayleigh-wave sensitivity kernels suggest that our resolution begins to degrade at about 150 km (Figure S21), so we do not image the entire feature. Nyamwandha et al. (2016) suggested that a Cretaceous thermal event producing these anomalies is associated with upwelling fluids from the Farallon Slab, along with an already weakened and thinned lithosphere as a result of interaction with the Bermuda Hot Spot roughly 80-100 Ma (Cox & Van Arsdale, 2002). The crustal thickness is a maximum beneath the Valley and Ridge and decreases by about 10 km at the coastal region to the east. Although not associated with seismicity, the cross-section indicates relatively higher mid-crust speeds beneath the Piedmont region of North Carolina.

Seismicity in the ETSZ occurs on basement faults that have no surface expression (Steltenpohl et al., 2010). Seismicity is located in the Valley and Ridge Province west of the highest Appalachian elevations. A recent local earthquake tomography study imaged the existence of the buried fault (Powell et al., 2014) as a low-velocity anomaly. The lateral extent of the low anomaly is beyond the resolution of our velocity model. Our model contains a velocity change in the lower crust beneath the ETSZ (ellipse in Figure 7), which may be associated with the transition from the Granite-Rhyolite basement (west) to the Grenville basement (east) (Fisher et al., 2010). Upper mantle shear velocity beneath the region is 2-3% faster than the mantle beneath the NMSZ at depths of about 100 km.

The northwest-southeast striking cross-section B1-B2 (Figure 8) shows apparently thinned crust beneath western North and South Dakota (solid ellipse) which is consistent with Thurner et al. (2015) who argued that the apparently thin crust is actually a very fast underplated crust in the vicinity of the 2 Ga Trans-Hudson Orogen. The model at what could be considered uppermost mantle depths is relatively slow, so it is plausible to interpret the material as fast crust. A region of apparently thin crust in southeastern North Dakota is more perplexing. Thurner et al. (2015) estimated a crustal thickness of 30-35 km in this region. Our apparent crustal thickness is slightly larger, about 38-40 km. To be fair, reverberations in the thin surface sedimentary cover interfere with the Ps arrival from the apparent crust-mantle boundary, which may affect an accurate estimation of the crust-mantle boundary. The multiples in receiver functions from the apparent crust-mantle boundary are free of near-surface interference, which provide some contraints on the boundary. The P-wave speeds in the apparent lower crust are in the 6.6-7.0 km/s range, not unusual, and the values increase to 7.8 sharply and reach values of 8.0-8.1 km/s by a depth of 43 km. The region has relatively low heat flow (50-60 mW/m^2, Blackwell et al., 2011) though the data coverage is sparse. The apparently thinned crust may be a result of eclogite facies mafic material in the lowermost crust rendering the petrologic crust-mantle boundary seismically transparent (Furlong & Fountain, 1986; Griffin & O'Reilly, 1987). In cratonic areas, eclogite facies mafic material in the lowermost crust can have a P-wave speed larger than 8 km/s, which can lead to bias in the estimation of the crust-mantle boundary. Near the South Dakota Iowa border, the mid-crustal shear wave speed decreases relatively abruptly. The relatively slow mid-crust (see also in Visualization S1) from Iowa through Missouri may be related to a batholith inferred from the Missouri gravity low (Hildenbrand et al., 1996). The structure from Iowa through Missouri is relatively uniform until interrupted by the relatively fast lower crust beneath the NMSZ. The upper mantle beneath Iowa and Missouri is relatively fast and uniform across this region of relatively slow middle crust. To the southeast of the NMSZ, the middle crust again is relatively slow and the crust begins to thin (dashed ellipse in Figure 8) and the upper crust speed decreases near the Alabama-Georgia Border. The upper mantle below 100 km, from the NMSZ to the southeast is one of the slowest profiles in the model, and includes the region believed to have been crossed by the Bermuda Hot Spot (Chu et al., 2013; Cox & Van Arsdale, 2002).

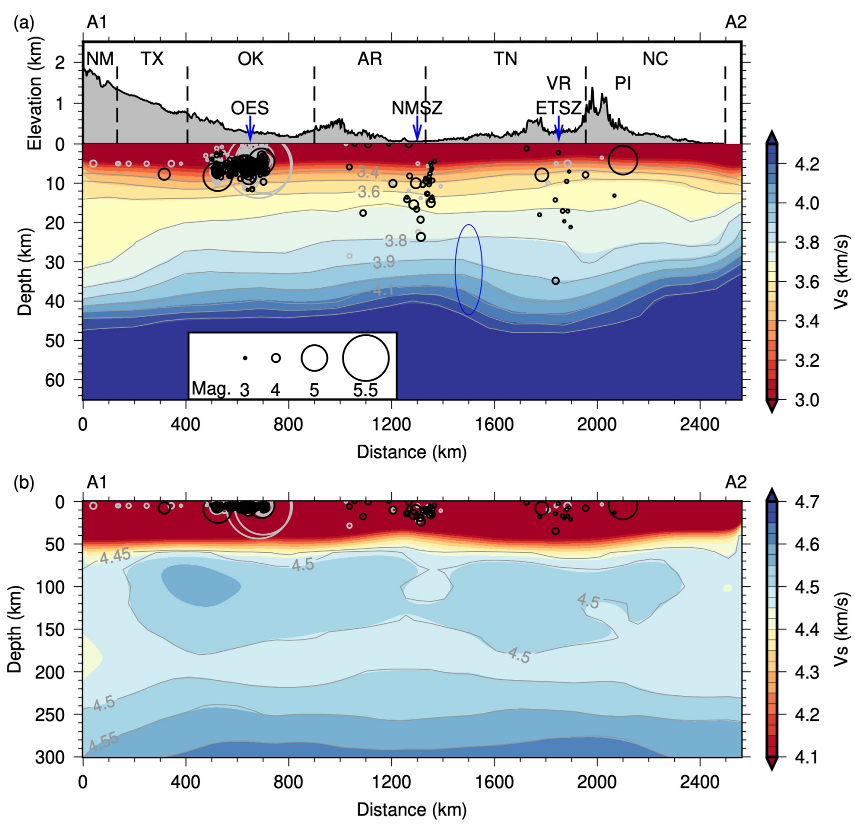

Figure 7. Shear velocity cross-sections along A1-A2. The panel (a) used a color palette for suitable crustal speeds. The panel (b) shows shear-wave speed changes in the upper mantle. Circles are earthquakes located within 100 km of the cross-section. Black circles are events with depth uncertainties less than 5 km. Gray circles represent earthquakes with larger depth uncertainties or without uncertainties. Note the image is vertically exaggerated.

Additional cross-sections can be found in Figure S22-S25 and discussed in Text S1. The inverted 3D seismic velocity model for the eastern United States is available in Data Set S1. The 3D seismic velocity model for the western United States from Chai et al. (2015) is provided in Data Set S2. We also provide an interactive tool (Chai et al., 2018) to easily view the 3D model with depth slides and depth profiles side by side for both the eastern United States (Visualization S1) and the western United States (Visualization S2).

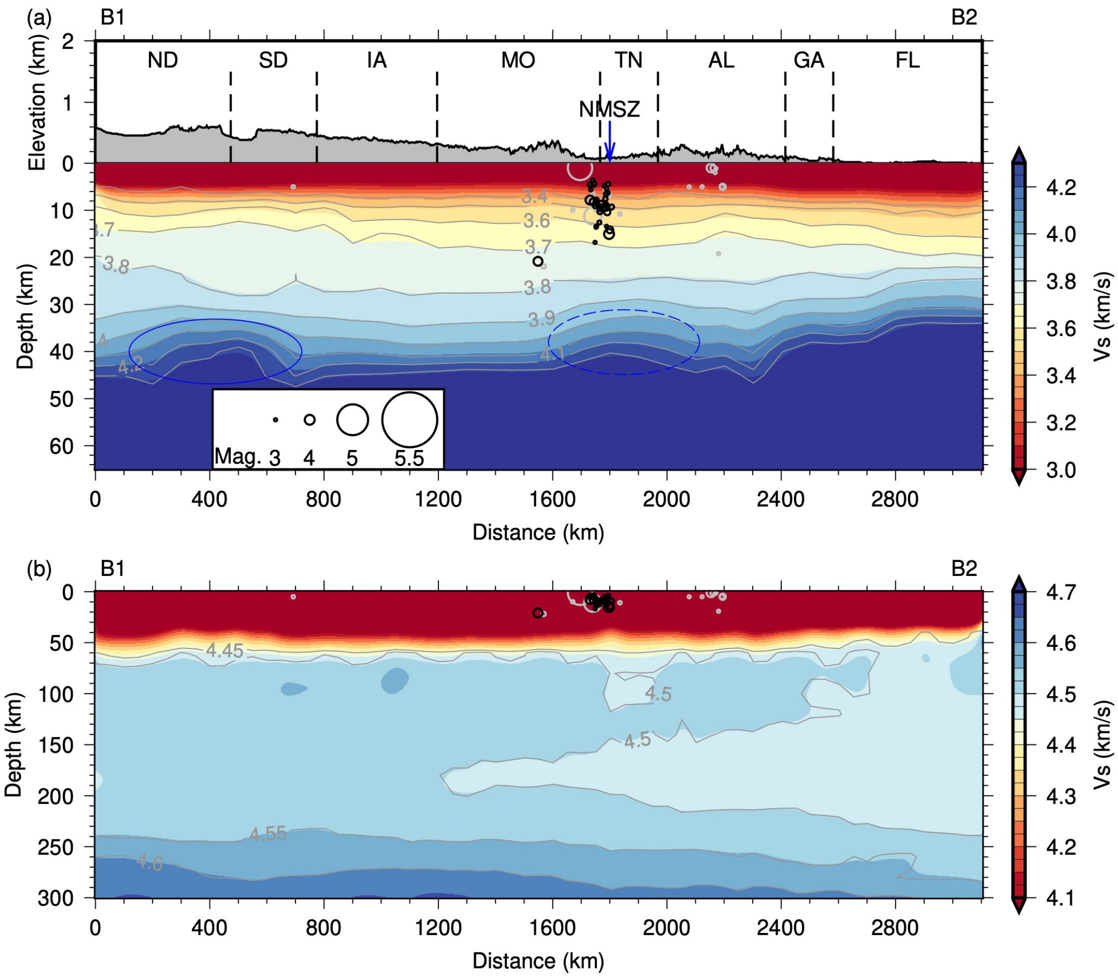

Figure 8. Same as Figure 7 but for cross-section B1-B2. The ellipses indicate anomalies described in the text.

7 Conclusions

Using spatially smoothed P-wave receiver functions, surface-wave dispersion, and Bouguer gravity observations, we construct 3D shear-wave velocity models in the EUS. The average crustal thickness of the EUS model is 43 km; the average crustal shear speed is 3.7 km/s; the average uppermost mantle shear-wave velocity in the model is 4.5 km/s. We imaged thinner crust beneath New England, the east coast, and the ME. The relative slow average shear-wave speeds in the mantle beneath New England and the southeastern US may be linked to hotspots.

Comparing to a compilation of basement age (Lund et al., 2015), regions with thin crust were formed after 670 Ma, thicker crust in the cratonic region formed before 1000 Ma.

A comparison of seismicity and subsurface shear velocity suggests that often, but not universally, earthquakes locate near regions with seismic velocity variation. However, not all regions of significant subsurface seismic speed changes are loci of seismicity. The eastern seaboard mantle appears slow, consistent with coarser, but deeper sampling models that have been used as a basis for estimating dynamic topographic changes along the eastern seaboard (Rowley et al., 2013). A weak correlation between upper mantle shear velocity and earthquake focal mechanism has been observed. A relatively small upper mantle low-speed region in eastern Kentucky and southwestern Ohio correlates with the area of perturbed upper mantle P-waves analyzed by (Chu et al., 2013) which they associated with the circa 75 Ma kimberlite volcanic site near Elliot Kentucky. The northern ME, and in particular the region of the large earthquakes in 1811-12 appears to be underlain by a relatively fast lower crust and a relatively slow uppermost mantle. Levandowski et al. (2016) suggested that such a structure can focus stress in the upper crust, and our model is consistent with the idea.

Acknowledgments, Samples, and Data

Initial analyses for this work were performed at Pennsylvania State University. This work was supported by the U.S. National Science Foundation (grants EAR-1053484 and EAR-1053363) and by the U.S. Department of Energy (DOE), Office of Fossil Energy, Carbon Storage Program through the Science-informed Machine Learning for Accelerating Real-Time Decisions in Subsurface Applications (SMART) Initiative. The facilities of IRIS Data Services, and specifically the IRIS Data Management Center, were used for access the waveforms, related metadata, and/or derived products used in this study. See Table S1 for a full list of seismic networks used in this study. IRIS Data Services are funded through the Seismological Facilities for the Advancement of Geoscience and EarthScope (SAGE) Proposal of the National Science Foundation under Cooperative Agreement EAR-1261681. Earthquake catalogs from U.S. Geological Survey (https://earthquake.usgs.gov/earthquakes/search/, last accessed July, 2021) and Saint Louis Univeristy Earthquake Center (Herrmann et al., 2011) were used in this study. We acknowledge developers of Generic Mapping Tools version 5.4.4 (Paul Wessel et al., 2013) and version 6.1.1 (P. Wessel et al., 2019), Obspy version 1.2.2 (Beyreuther et al., 2010; Krischer et al., 2015; Megies et al., 2011), Numpy version 1.20.1 (Van Der Walt et al., 2011), Matplotlib version 3.3.3 (Hunter, 2007), and Scikit-learn version 0.24.2 (Pedregosa et al., 2011) for sharing their software packages. We thank University of California San Diego for sharing the STRM15 topography data that were used as background for several figures. We also thank National Centers for Environmental Information for making ETOPO Global Relief Model available. The boundaries of sedimentary basins were extracted from Coleman Jr. & Cahan (2012). This manuscript has been authored in part by UT-Battelle, LLC, under contract DE- AC05-00OR22725 with the US Department of Energy (DOE). The US government retains and the publisher, by accepting the article for publication, acknowledges that the US government retains a nonexclusive, paid-up, irrevocable, worldwide license to publish or reproduce the published form of this manuscript, or allow others to do so, for US government purposes. DOE will provide public access to these results of federally sponsored research in accordance with the DOE Public Access Plan (http://energy.gov/downloads/doe-public-access-plan, last accessed in May 2021). The views and conclusions contained in this document are those of the authors and should not be interpreted as necessarily representing the official policies, either expressed or implied, of the U.S. Government. The authors declare that they have no conflict of interest. The authors thank the Editor Maureen Long, Brian Savage, and an anonymous reviewer for their constructive comments.

References

Ammon, C. J. (1991). The isolation of receiver effects from teleseismic P -waveforms. *Bulletin of the Seismological Society of America*. https://doi.org/10.1029/2005JB004161

Ammon, C. J., Randall, G. E., & Zandt, G. (1990). On the nonuniqueness of receiver function inversions. *Journal of Geophysical Research*, *95*(B10), 15303. https://doi.org/10.1029/JB095iB10p15303

Balmino, G., Vales, N., Bonvalot, S., & Briais, A. (2012). Spherical harmonic modelling to ultra-high degree of Bouguer and isostatic anomalies. *Journal of Geodesy*, *86*(7), 499–520. https://doi.org/10.1007/s00190-011-0533-4

Bensen, G. D., Ritzwoller, M. H., Barmin, M. P., Levshin, A. L., Lin, F., Moschetti, M. P., et al. (2007). Processing seismic ambient noise data to obtain reliable broad-band surface wave dispersion measurements. *Geophysical Journal International*, *169*(3), 1239–1260. https://doi.org/10.1111/j.1365-246X.2007.03374.x

Beyreuther, M., Barsch, R., Krischer, L., Megies, T., Behr, Y., & Wassermann, J. (2010). ObsPy: A Python Toolbox for Seismology. *Seismological Research Letters*, *81*(3), 530–533. https://doi.org/10.1785/gssrl.81.3.530

Biryol, C. B., Wagner, L. S., Fischer, K. M., & Hawman, R. B. (2016). Relationship between observed upper mantle structures and recent tectonic activity across the Southeastern United States. *Journal of Geophysical Research: Solid Earth*, *121*(5), 3393–3414. https://doi.org/10.1002/2015JB012698

Biswas, N. N. (1972). Earth-flattening procedure for the propagation of Rayleigh wave. *Pure and Applied Geophysics PAGEOPH*, *96*(1), 61–74. https://doi.org/10.1007/BF00875629

Blackwell, D., Richards, M., Frone, Z., Batir, J., Ruzo, A., Dingwall, R., & Williams, M. (2011). Temperature at depth maps for the conterminous US and geothermal resource estimates. *Geothermal Resources Council Transactions 35*, 1545–1550.

Bollmann, T. A., van der Lee, S., Frederiksen, A. W., Wolin, E., Revenaugh, J., Wiens, D. A., et al. (2019). P Wave Teleseismic Traveltime Tomography of the North American Midcontinent. *Journal of Geophysical Research: Solid Earth*, *124*(2), 1725–1742. https://doi.org/10.1029/2018JB016627

Catchings, R. D. (1999). Regional Vp, Vs, Vp/Vs, and Poisson's ratios across earthquake source zones from Memphis, Tennessee, to St. Louis, Missouri. *Bulletin of the Seismological Society of America*.

Chai, C., Ammon, C. J., Maceira, M., & Herrmann, R. B. (2015). Inverting interpolated receiver functions with surface wave dispersion and gravity: Application to the western U.S. and adjacent Canada and Mexico. *Geophysical Research Letters*, *42*(11), 4359–4366. https://doi.org/10.1002/2015GL063733

Chai, C., Ammon, C. J., Anandakrishnan, S., Ramirez, C., & Nyblade, A. (2017). Estimating subglacial structure using P-wave receiver functions. *Geophysical Journal International*, *209*(2), 1064–1079. https://doi.org/10.1093/gji/ggx075

Chai, C., Ammon, C. J., Maceira, M., & Herrmann, R. B. (2018). Interactive Visualization of Complex Seismic Data and Models Using Bokeh. *Seismological Research Letters*, *89*(2A), 668–676. https://doi.org/10.1785/0220170132

Chai, C., Delorey, A. A., Maceira, M., Levandowski, W., Guyer, R. A., Zhang, H., et al. (2021). A 3D Full Stress Tensor Model for Oklahoma. *Journal of Geophysical Research: Solid Earth*, *126*(4), e2020JB021113. https://doi.org/10.1029/2020JB021113

Chen, Chen, Gilbert, H., Andronicos, C., Hamburger, M. W., Larson, T., Marshak, S., et al. (2016). Shear velocity structure beneath the central United States: implications for the origin of the Illinois Basin and intraplate seismicity. *Geochemistry, Geophysics, Geosystems*, *17*(3), 1020–1041. https://doi.org/10.1002/2015GC006206

Chen, Chuanxu, Zhao, D., & Wu, S. (2014). Crust and upper mantle structure of the New Madrid Seismic Zone: Insight into intraplate earthquakes. *Physics of the Earth and Planetary Interiors*, *230*, 1–14. https://doi.org/10.1016/j.pepi.2014.01.016

Chong, J., Ni, S., Chu, R., & Somerville, P. (2016). Joint Inversion of Body-Wave Receiver Function and Rayleigh-Wave Ellipticity. *Bulletin of the Seismological Society of America*, *106*(2), 537–551. https://doi.org/10.1785/0120150075

Christensen, N. I., & Mooney, W. D. (1995). Seismic velocity structure and composition of the continental crust: A global view. *Journal of Geophysical Research: Solid Earth*, *100*(B6), 9761–9788. https://doi.org/10.1029/95JB00259

Chu, R., Leng, W., Helmberger, D. V., & Gurnis, M. (2013). Hidden hotspot track beneath the eastern United States. *Nature Geoscience*, *6*(11), 963–966. https://doi.org/10.1038/ngeo1949

Coleman Jr., J. L., & Cahan, S. M. (2012). *Preliminary catalog of the sedimentary basins of the United States*. Reston, VA. https://doi.org/10.3133/ofr20121111

Constable, S. C., Parker, R. L., & Constable, C. G. (1987). Occam's inversion: A practical algorithm for generating smooth models from electromagnetic sounding data. *GEOPHYSICS*, *52*(3), 289–300. https://doi.org/10.1190/1.1442303

Cox, R. T., & Van Arsdale, R. B. (2002). The Mississippi Embayment, North America: a first order continental structure generated by the Cretaceous superplume mantle event. *Journal of Geodynamics*, *34*(2), 163–176. https://doi.org/10.1016/S0264-3707(02)00019-4

Crotwell, H. P., & Owens, T. J. (2005). Automated Receiver Function Processing. *Seismological Research Letters*, *76*(6), 702–709. https://doi.org/10.1785/gssrl.76.6.702

Dong, M. T., & Menke, W. H. (2017). Seismic High Attenuation Region Observed Beneath Southern New England From Teleseismic Body Wave Spectra: Evidence for High Asthenospheric Temperature Without Melt. *Geophysical Research Letters*, *44*(21), 10,958-10,969. https://doi.org/10.1002/2017GL074953

Eaton, D. W., & Frederiksen, A. (2007). Seismic evidence for convection-driven motion of the North American plate. *Nature*, *446*(7134), 428–431. https://doi.org/10.1038/nature05675

Ekström, G. (2011). A global model of Love and Rayleigh surface wave dispersion and anisotropy, 25-250 s. *Geophysical Journal International*, *187*(3), 1668–1686. https://doi.org/10.1111/j.1365-246X.2011.05225.x

Ekström, G. (2014). Love and Rayleigh phase-velocity maps, 5–40 s, of the western and central USA from USArray data. *Earth and Planetary Science Letters*, *402*, 42–49. https://doi.org/10.1016/j.epsl.2013.11.022

Faill, R. T. (1998). A geologic history of the north-central Appalachians; Part 3, The Alleghany Orogeny. *American Journal of Science*, *298*(2), 131–179. https://doi.org/10.2475/ajs.298.2.131

Fisher, C. M., Loewy, S. L., Miller, C. F., Berquist, P., Van Schmus, W. R., Hatcher, R. D., et al. (2010). Whole-rock Pb and Sm-Nd isotopic constraints on the growth of southeastern Laurentia during Grenvillian orogenesis. *Geological Society of America Bulletin*, *122*(9–10), 1646–1659. https://doi.org/10.1130/B30116.1

Furlong, K. P., & Fountain, D. M. (1986). Continental crustal underplating: Thermal considerations and seismic-petrologic consequences. *Journal of Geophysical Research*, *91*(B8), 8285. https://doi.org/10.1029/JB091iB08p08285

Golos, E. M., Fang, H., Yao, H., Zhang, H., Burdick, S., Vernon, F., et al. (2018). Shear Wave Tomography Beneath the United States Using a Joint Inversion of Surface and Body Waves. *Journal of Geophysical Research: Solid Earth*, *123*(6), 5169–5189. https://doi.org/10.1029/2017JB014894

Grana, J. P., & Richardson, R. M. (1996). Tectonic stress within the New Madrid seismic zone. *Journal of Geophysical Research: Solid Earth*, *101*(B3), 5445–5458. https://doi.org/10.1029/95JB03255

Griffin, W. L., & O’Reilly, S. Y. (1987). Is the continental Moho the crust-mantle boundary? *Geology*, *15*(3), 241. https://doi.org/10.1130/0091-7613(1987)15<241:ITCMTC>2.0.CO;2

Grollimund, B., & D. Zoback, M. (2001). Did deglaciation trigger intraplate seismicity in the New Madrid seismic zone? *Geology*, *29*(2), 175. https://doi.org/10.1130/0091-7613(2001)029<0175:DDTISI>2.0.CO;2

Hames, W. E., Renne, P. R., & Ruppel, C. (2000). New evidence for geologically instantaneous emplacement of earliest Jurassic Central Atlantic magmatic province basalts on the North American margin. *Geology*, *28*(9), 859. https://doi.org/10.1130/0091-7613(2000)28<859:NEFGIE>2.0.CO;2

Hatcher, R. D. (2010). The Appalachian orogen: A brief summary (pp. 1–19). https://doi.org/10.1130/2010.1206(01)

Herrmann, R. B., Benz, H., & Ammon, C. J. (2011). Monitoring the Earthquake Source Process in North America. *Bulletin of the Seismological Society of America*, *101*(6), 2609–2625. https://doi.org/10.1785/0120110095

Herrmann, R. B., Ammon, C. J., Benz, H. M., Aziz-Zanjani, A., & Boschelli, J. (2021). Short-Period Surface-Wave Tomography in the Continental United States—A Resource for Research. *Seismological Research Letters*, *92*(6), 3642–3656. https://doi.org/10.1785/0220200462

Hildenbrand, T. G., Griscom, A., Van Schmus, W. R., & Stuart, W. D. (1996). Quantitative investigations of the Missouri gravity low: A possible expression of a large, Late Precambrian batholith intersecting the New Madrid seismic zone. *Journal of Geophysical Research: Solid Earth*, *101*(B10), 21921–21942. https://doi.org/10.1029/96JB01908

Hough, S. E., Armbruster, J. G., Seeber, L., & Hough, J. F. (2000). On the Modified Mercalli intensities and magnitudes of the 1811-1812 New Madrid earthquakes. *Journal of Geophysical Research: Solid Earth*, *105*(B10), 23839–23864. https://doi.org/10.1029/2000JB900110

Hunter, J. D. (2007). Matplotlib: a 2D graphics environment. *Computing in Science & Engineering*, *9*(3), 90–95. https://doi.org/10.1109/MCSE.2007.55

Hynes, A., & Rivers, T. (2010). Protracted continental collision - evidence from the Grenville Orogen. *Canadian Journal of Earth Sciences*, *47*(5), 591–620. https://doi.org/10.1139/E10-003

Jin, G., & Gaherty, J. B. (2015). Surface wave phase-velocity tomography based on multichannel cross-correlation. *Geophysical Journal International*, *201*(3), 1383–1398. https://doi.org/10.1093/gji/ggv079

Johnston, A. C. (1996). Seismic moment assessment of earthquakes in stable continental regions-III. New Madrid 1811-1812, Charleston 1886 and Lisbon 1755. *Geophysical Journal International*, *126*(2), 314–344. https://doi.org/10.1111/j.1365-246X.1996.tb05294.x

Julià, J., Ammon, C. J., Herrmann, R. B., & Correig, A. M. (2000). Joint inversion of receiver function and surface wave dispersion observations. *Geophysical Journal International*, *143*(1), 99–112. https://doi.org/10.1046/j.1365-246x.2000.00217.x

Julià, J., Ammon, C. J., & Herrmann, R. B. (2003). Lithospheric structure of the Arabian Shield from the joint inversion of receiver functions and surface-wave group velocities.

Tectonophysics, *371*(1–4), 1–21. https://doi.org/10.1016/S0040-1951(03)00196-3

Kenner, S. J. (2000). A Mechanical Model for Intraplate Earthquakes: Application to the New Madrid Seismic Zone. *Science*, *289*(5488), 2329–2332. https://doi.org/10.1126/science.289.5488.2329

Kennett, B. L. N., Engdahl, E. R., & Buland, R. (1995). Constraints on seismic velocities in the Earth from traveltimes. *Geophysical Journal International*, *122*(1), 108–124. https://doi.org/10.1111/j.1365-246X.1995.tb03540.x

Krischer, L., Megies, T., Barsch, R., Beyreuther, M., Lecocq, T., Caudron, C., & Wassermann, J. (2015). ObsPy: a bridge for seismology into the scientific Python ecosystem. *Computational Science & Discovery*, *8*(1), 014003. https://doi.org/10.1088/1749-4699/8/1/014003

Langston, C. A. (1979). Structure under Mount Rainier, Washington, inferred from teleseismic body waves. *Journal of Geophysical Research*, *84*(B9), 4749. https://doi.org/10.1029/JB084iB09p04749

Langston, C. A. (2011). Wave-Field Continuation and Decomposition for Passive Seismic Imaging Under Deep Unconsolidated Sediments. *Bulletin of the Seismological Society of America*, *101*(5), 2176–2190. https://doi.org/10.1785/0120100299

Laske, G., Masters, G., Ma, Z., & Pasyanos, M. (2013). Update on CRUST1. 0-A 1-degree global model of Earth's crust. *EGU General Assembly*, *15*, 2658.

Levandowski, W., Boyd, O. S., & Ramirez-Guzmán, L. (2016). Dense lower crust elevates long-term earthquake rates in the New Madrid seismic zone. *Geophysical Research Letters*, *43*(16), 8499–8510. https://doi.org/10.1002/2016GL070175

Li, Q., Liu, M., Zhang, Q., & Sandvol, E. (2007). Stress evolution and seismicity in the central-eastern United States: Insights from geodynamic modeling. In *Special Paper 425: Continental Intraplate Earthquakes: Science, Hazard, and Policy Issues* (pp. 149–166). Geological Society of America. https://doi.org/10.1130/2007.2425(11)

Ligorría, J. P., & Ammon, C. J. (1999). Iterative deconvolution and receiver-function estimation. *Bulletin of the Seismological Society of America*, *89*(5), 1395–1400.

Lund, K., Box, S. E., Holm-Denoma, C., San Juan, C. A., Blakely, R. J., Saltus, R. W., et al. (2015). *Basement Domain Map of the Conterminous United States and Alaska*. *U.S. Geological Survey Data Series 898*. https://doi.org/10.3133/ds898

Maceira, M., & Ammon, C. J. (2009). Joint inversion of surface wave velocity and gravity observations and its application to central Asian basins shear velocity structure. *Journal of Geophysical Research*, *114*(B2), B02314. https://doi.org/10.1029/2007JB005157

Mazza, S. E., Gazel, E., Johnson, E. A., Kunk, M. J., McAleer, R., Spotila, J. A., et al. (2014). Volcanoes of the passive margin: The youngest magmatic event in eastern North America.

Geology, *42*(6), 483–486. https://doi.org/10.1130/G35407.1

Megies, T., Beyreuther, M., Barsch, R., Krischer, L., & Wassermann, J. (2011). ObsPy - what can it do for data centers and observatories? *Annals of Geophysics*, *54*(1), 47–58. https://doi.org/10.4401/ag-4838

Menke, W., Lamoureux, J., Abbott, D., Hopper, E., Hutson, D., & Marrero, A. (2018). Crustal Heating and Lithospheric Alteration and Erosion Associated With Asthenospheric Upwelling Beneath Southern New England (USA). *Journal of Geophysical Research: Solid Earth*, *123*(10), 8995–9008. https://doi.org/10.1029/2018JB015921

Mooney, W. D., Andrews, M. C., Ginzburg, A., Peters, D. A., & Hamilton, R. M. (1983). Crustal Structure of the Northern Mississippi Embayment and a Comparison with other Continental Rift Zones. In *Developments in Geotectonics* (pp. 327–348). https://doi.org/10.1016/B978-0-444-42198-2.50025-0

Newman, A. (1999). Slow Deformation and Lower Seismic Hazard at the New Madrid Seismic Zone. *Science*, *284*(5414), 619–621. https://doi.org/10.1126/science.284.5414.619

Nyamwandha, C. A., Powell, C. A., & Langston, C. A. (2016). A joint local and teleseismic tomography study of the Mississippi Embayment and New Madrid Seismic Zone. *Journal of Geophysical Research: Solid Earth*, *121*(5), 3570–3585. https://doi.org/10.1002/2015JB012761

Özalaybey, S., Savage, M. K., Sheehan, A. F., Louie, J. N., & Brune, J. N. (1997). Shear-wave velocity structure in the northern Basin and Range province from the combined analysis of receiver functions and surface waves. *Bulletin of the Seismological Society of America*, *87*(1), 183–199.

Paige, C. C., & Saunders, M. A. (1982). LSQR: An Algorithm for Sparse Linear Equations and Sparse Least Squares. *ACM Transactions on Mathematical Software*, *8*(1), 43–71. https://doi.org/10.1145/355984.355989

Pavlis, N. K., Holmes, S. A., Kenyon, S. C., & Factor, J. K. (2012). The development and evaluation of the Earth Gravitational Model 2008 (EGM2008). *Journal of Geophysical Research: Solid Earth*, *117*(B4), B04406. https://doi.org/10.1029/2011JB008916

Pedregosa, F., Varoquaux, G., Gramfort, A., Michel, V., Thirion, B., Grisel, O., et al. (2011). Scikit-learn: Machine Learning in Python. *Journal of Machine Learning Research*, *12*, 2825–2830.

Plouff, D. (1976). Gravity and magnetic fields of polygonal prisms and application to magnetic terrain corrections. *Geophysics*, *41*(4), 727–741. https://doi.org/10.1190/1.1440645

Pollitz, F. F. (2001). Sinking Mafic Body in a Reactivated Lower Crust: A Mechanism for Stress Concentration at the New Madrid Seismic Zone. *Bulletin of the Seismological Society of America*, *91*(6), 1882–1897. https://doi.org/10.1785/0120000277

Pollitz, F. F., & Mooney, W. D. (2014). Seismic structure of the Central US crust and shallow upper mantle: Uniqueness of the Reelfoot Rift. *Earth and Planetary Science Letters*, *402*, 157–166. https://doi.org/10.1016/j.epsl.2013.05.042

Porter, R., Liu, Y., & Holt, W. E. (2016). Lithospheric records of orogeny within the continental U.S. *Geophysical Research Letters*, *43*(1), 144–153. https://doi.org/10.1002/2015GL066950

Powell, C. A., Withers, M. M., Cox, R. T., Vlahovic, G., & Arroucau, P. (2014). Crustal velocity structure associated with the eastern Tennessee seismic zone: Vp and Vs images based upon local earthquake tomography. *Journal of Geophysical Research: Solid Earth*, *119*(1), 464–489. https://doi.org/10.1002/2013JB010433

Rowley, D. B., Forte, A. M., Moucha, R., Mitrovica, J. X., Simmons, N. A., & Grand, S. P. (2013). Dynamic topography change of the Eastern United States since 3 million years ago. *Science*, *340*(6140), 1560–1563. https://doi.org/10.1126/science.1229180

Saito, M. (1988). Disper80: A subroutine package for the calculation of seismic normal-mode solutions. In *Seismological algorithms* (pp. 293–319). Academic Press.

Savage, B., Covellone, B. M., & Shen, Y. (2017). Wave speed structure of the eastern North American margin. *Earth and Planetary Science Letters*, *459*, 394–405. https://doi.org/10.1016/j.epsl.2016.11.028

Savage, Brian. (2021). Body Wave Speed Structure of Eastern North America. *Geochemistry, Geophysics, Geosystems*, *22*(1), 1–18. https://doi.org/10.1029/2020GC009002

Schmandt, B., Lin, F.-C., & Karlstrom, K. E. (2015). Distinct crustal isostasy trends east and west of the Rocky Mountain Front. *Geophysical Research Letters*, *42*(23), 10,290-10,298. https://doi.org/10.1002/2015GL066593

Shen, W., & Ritzwoller, M. H. (2016). Crustal and uppermost mantle structure beneath the United States. *Journal of Geophysical Research: Solid Earth*, *121*(6), 4306–4342. https://doi.org/10.1002/2016JB012887

Stein, S. (2007). Approaches to continental intraplate earthquake issues. In *Special Paper 425: Continental Intraplate Earthquakes: Science, Hazard, and Policy Issues* (pp. 1–16). Geological Society of America. https://doi.org/10.1130/2007.2425(01)

Steltenpohl, M. G., Zietz, I., Horton, J. W., & Daniels, D. L. (2010). New York–Alabama lineament: A buried right-slip fault bordering the Appalachians and mid-continent North America. *Geology*, *38*(6), 571–574. https://doi.org/10.1130/G30978.1

Sun, X., Bao, X., Xu, M., Eaton, D. W., Song, X., Wang, L., et al. (2014). Crustal structure beneath SE Tibet from joint analysis of receiver functions and Rayleigh wave dispersion. *Geophysical Research Letters*, *41*(5), 1479–1484. https://doi.org/10.1002/2014GL059269

Thurner, S., Margolis, R., Levander, A., & Niu, F. (2015). PdS receiver function evidence for crustal scale thrusting, relic subduction, and mafic underplating in the Trans-Hudson

Orogen and Yavapai province. *Earth and Planetary Science Letters*, *426*, 13–22. https://doi.org/10.1016/j.epsl.2015.06.007

Tuttle, M. P. (2002). The Earthquake Potential of the New Madrid Seismic Zone. *Bulletin of the Seismological Society of America*, *92*(6), 2080–2089. https://doi.org/10.1785/0120010227

Wagner, L. S., Fischer, K. M., Hawman, R., Hopper, E., & Howell, D. (2018). The relative roles of inheritance and long-term passive margin lithospheric evolution on the modern structure and tectonic activity in the southeastern United States. *Geosphere*, *14*(4), 1385–1410. https://doi.org/10.1130/GES01593.1

Van Der Walt, S., Colbert, S. C., & Varoquaux, G. (2011). The NumPy array: A structure for efficient numerical computation. *Computing in Science and Engineering*, *13*(2), 22–30. https://doi.org/10.1109/MCSE.2011.37

Wessel, P., Luis, J. F., Uieda, L., Scharroo, R., Wobbe, F., Smith, W. H. F., & Tian, D. (2019). The Generic Mapping Tools Version 6. *Geochemistry, Geophysics, Geosystems*, *20*(11), 5556–5564. https://doi.org/10.1029/2019GC008515

Wessel, Paul, Smith, W. H. F., Scharroo, R., Luis, J., & Wobbe, F. (2013). Generic Mapping Tools: improved version released. *Eos, Transactions American Geophysical Union*, *94*(45), 409–410. https://doi.org/10.1002/2013EO450001

Whitmeyer, S. (2007). Tectonic model for the Proterozoic growth of North America. *Geosphere*, *3*(4), 220. https://doi.org/10.1130/GES00055.1

Yang, B. B., Gao, S. S., Liu, K. H., Elsheikh, A. A., Lemnifi, A. A., Refayee, H. A., & Yu, Y. (2014). Seismic anisotropy and mantle flow beneath the northern Great Plains of North America. *Journal of Geophysical Research: Solid Earth*, *119*(3), 1971–1985. https://doi.org/10.1002/2013JB010561

Yang, X., Pavlis, G. L., & Wang, Y. (2016). A Quality Control Method for Teleseismic P -Wave Receiver Functions. *Bulletin of the Seismological Society of America*, *106*(5), 1948–1962. https://doi.org/10.1785/0120150347

Zhan, Y., Hou, G., Kusky, T., & Gregg, P. M. (2016). Stress development in heterogenetic lithosphere: Insights into earthquake processes in the New Madrid Seismic Zone. *Tectonophysics*, *671*, 56–62. https://doi.org/10.1016/j.tecto.2016.01.016

Zhu, L. (2000). Crustal structure across the San Andreas Fault, southern California from teleseismic converted waves. *Earth and Planetary Science Letters*, *179*(1), 183–190. https://doi.org/10.1016/S0012-821X(00)00101-1

Zhu, L., & Kanamori, H. (2000). Moho depth variation in southern California from teleseismic receiver functions. *Journal of Geophysical Research: Solid Earth*, *105*(B2), 2969–2980. https://doi.org/10.1029/1999JB900322

Geochemistry, Geophysics, Geosystems

Supporting Information for

Crust and Upper Mantle Structure Beneath the Eastern United States

Chengping Chai[1], Charles J. Ammon[2], Monica Maceira[1], Robert Herrmann[3]

[1]Oak Ridge National Laboratory, Oak Ridge, Tennessee, U.S.A.

[2]Department of Geosciences, Pennsylvania State University, University Park, Pennsylvania, U.S.A.

[3]Department of Earth and Atmospheric Sciences, Saint Louis University, St. Louis, Missouri, U.S.A.

Contents of this file

Additional Supporting Information (Files uploaded separately)

Introduction

This supplement includes details on the formulas to convert seismic velocities to densities (Text S1); paragraphs describing cross-sections B1-B2, D1-D2, E1-E2, F1-F2, G1-G2, and H1-H2 (Text S2); a map showing the seismic stations used for receiver functions (Figure S1); a map showing the seismic events used for receiver functions (Figure S2); a figure showing the relative data variance of receiver functions (Figure S3); a figure showing example surface-wave dispersions (Figure S4); a figure showing Bouguer gravity maps before and after wavenumber filtering (Figure S5); a comparison of single-station receiver functions and smoothed receiver functions (Figure S6); a figure showing the convergence of the simultaneous inversion (Figure S7); a figure showing receiver function misfits (Figure S8); a figure showing surface-wave dispersion misfits (Figure S9); a comparison of the observed gravity maps and the predicted gravity maps (Figure S10); a comparison of EARS crust thickness before and after smoothing (Figure S11); a comparison of crustal thickness maps from recent seismic velocity models (Figure S12); a comparison of 1D velocity profiles (Figure S13); a figure showing the distributions of crustal and uppermost mantle P-wave velocities (Figure S14); a comparison of the uppermost mantle V_s and earthquake focal mechanisms (Figure S15); a comparison of the upper mantle shear speed at 63 km depth in western and easter U.S. (Figure S16); maps showing cluster locations (Figure S17 and S19); velocity profiles for each cluster (Figure S18 and S20); Rayleigh wave sensitivity kernels (Figure S21); V_s cross-section C1-C2 (Figure S22); V_s cross-section D1-D2 (Figure S23); V_s cross-section E1-E2 and F1-F2 (Figure S24); V_s cross-section G1-G2 and H1-H2 (Figure S25); the final seismic velocity model for the eastern United States in a text file (Data Set S1); the seismic velocity model for the western United States in a text file (Data Set S2); a list of seismic networks used in an excel file (Table S1); an animation compares the single-station-averaged receiver functions and the smoothed version (Movie S1); and interactive tools to view the seismic velocity model for the eastern United States (Visualization S1) and for the western United States (Visualization S2).

Text S1.

We used the following formulas from Maceira & Ammon (2009) to convert seismic velocities to densities.

$$\rho(\alpha) = \cos^2\phi\, \rho_2(\alpha) + \sin^2\phi\, \rho_1(\alpha)$$

$$\rho_1(\alpha) = \frac{\alpha + 2.40}{3.125}$$

$$\rho_2(\alpha) = \frac{7.55 - \sqrt{57.00 - 10.56(6.86 - \alpha)}}{5.28}$$

$$\phi = \frac{\pi}{2}\frac{1 + \tanh[\xi(\alpha - \alpha_c)]}{2}$$

In the formulas, ξ is 0.5 and α_c is 6.2 km/s. α is the seismic P wave velocity in km/s and ρ is density in g/cm^3.

Text S2.

The cross-section C1-C2 (Figure S22) is parallel to the longer arm of the New Madrid seismic zone (NMSZ) and passes through the Wabash Valley seismic zone (WVSZ) of Illinois and Indiana. Compared to the region to the north (left in Figure), the crust hosting modern WVSZ seismicity is relatively faster, with a smaller velocity gradient in the mid-to-lower crust. The WVSZ is underlain by a slightly thicker crust than the NMSZ. However, the upper mantle beneath the WVSZ is faster than that beneath the NMSZ. A broad higher velocity anomaly is imaged beneath the WVSZ about 70-150 km depth, which agrees with a recent local study (Chen Chen et al., 2016). The continuation of a relatively fast lower crust beneath the NMSZ northward to the WVSZ may suggest these two seismic active regions are connected (Chen Chen et al., 2016). To the south-southwest of the NMSZ, deeper into the Mississippi Embayment, the sedimentary cover thickens to at least 10 km and the crust thins to roughly 30 km.

The cross-section D1-D2, E1-E2, F1-F2, G1-G2, and H1-H2 pass through and across the Appalachian Mountains. Cross-section D1-D2 (Figure S23) clearly shows a slower upper mantle beneath New England, which is consistent with other studies (Pollitz & Mooney, 2016; Schmandt et al., 2015; Shen & Ritzwoller, 2016). The decrease seismic velocity has been interpreted as due to interaction with the Great Meteor hotspot roughly 50 Ma (Eaton & Frederiksen, 2007). Along the profile, which samples the Valley and Ridge Province of central and eastern Pennsylvania, the crustal thickness increases by roughly 10 km from eastern Pennsylvania into the West-Virginia border. Crustal thicknesses in western Pennsylvania are comparable to those to the south (see Figure 5). Although the mid crust varies in speed along the profile, the change in crustal thickness appears to arise from an increase in thickness of lower crustal material. Depths of earthquakes along the profile are generally above 25 kilometers and show no systematic variation with the structure.

Cross-section E1-E2 (Figure S24) samples from southeastern Canada into New England and crosses the West Quebec seismic zone (WQSZ). Magnitude 3 and larger earthquakes extend to 20 km depth in the WQSZ region and appear to shallow slightly along the profile in New York and New England. Along this direction, the WQSZ locates near the edge of the Canadian Shield as is evident in the mantle speed cross-section. Cross-section F1-F2 (Figure S24) shows a crustal thickness change beneath central Pennsylvania. Crossing from the Appalachian Plateau to the Valley and Ridge Province, the upper crust slows and the lower crust thins. At roughly the same position the mantle speeds decrease. Seismicity in the region shows transitions from reverse faulting in the thinner southeast part of the state to strike-slip faulting in the northwest. Whether the stress change is associated with the structure within the crust and/or upper mantle is difficult to tell. The pattern of reverse faulting continues down the eastern seaboard along the area of relatively thin crust. But reverse faulting in northern New York and southeastern Canada occurs with crust with more typical interior thicknesses. The pattern is slightly better matched with reverse faulting occurring above the regions of the relatively slow uppermost mantle (Figure S24), so perhaps the change (from South Carolina to Ottawa) is a result of an overall variation in lithospheric strength.

Cross-section G1-G2 (Figure S25) crosses eastern Ohio and through central Virginia and into northwestern North Carolina. Crustal thickness in eastern Ohio is comparable to that under the Appalachians, or perhaps slightly thinner. As discussed earlier in the Results section, the crustal thickness changes quickly as you exit the Appalachians to the east. Mantle speeds decrease modestly, but steadily from Ohio to the Appalachians. The 2011 M5.7 Virginia earthquake was located near an edge of a faster lower crust anomaly (the solid ellipse in Figure S25) and a change in crustal and upper mantle structure. Cross-section H1-H2 (Figure S25) crosses from the northeast WVSZ to the Charleston region and the South Carolina Seismic Zone. The crustal thickness increases slightly from the midwest into the Appalachians, and seismicity appears to extend slightly deeper in the

ETSZ near the profile. Near the southeastern margin of the Appalachians, into the coastal plain, the depth range of slower crustal material increases. The material that could be called lower-mid crust in the midwest and Appalachians disappears as the material with typical lower-crustal speeds shallows with a thinning of the crust. At the same position, the mantle speeds decrease along the east coast. Mantle speeds decrease modestly, but steadily from Indiana to the Appalachians, crossing the region that (Chu et al., 2013) suggested a hidden hot-spot track. Along the profile, we see no evidence for a slow upper mantle. However, our model includes a slight reduction in average upper mantle speed in northeast Kentucky and southwest Ohio (see Figure 6), directly above the turning points of the rays that showed delayed travel times and frequency-dependent amplitudes analyzed by (Chu et al., 2013) (the signals were generated by the Virginia earthquake and recorded on midwest Transportable Array stations described in that work). The slow upper mantle anomaly in our model is shallower than where they placed the anomaly but may reflect the same feature. However, we do not see it extend to the west, towards the northern Mississippi Embayment, as they suggested.

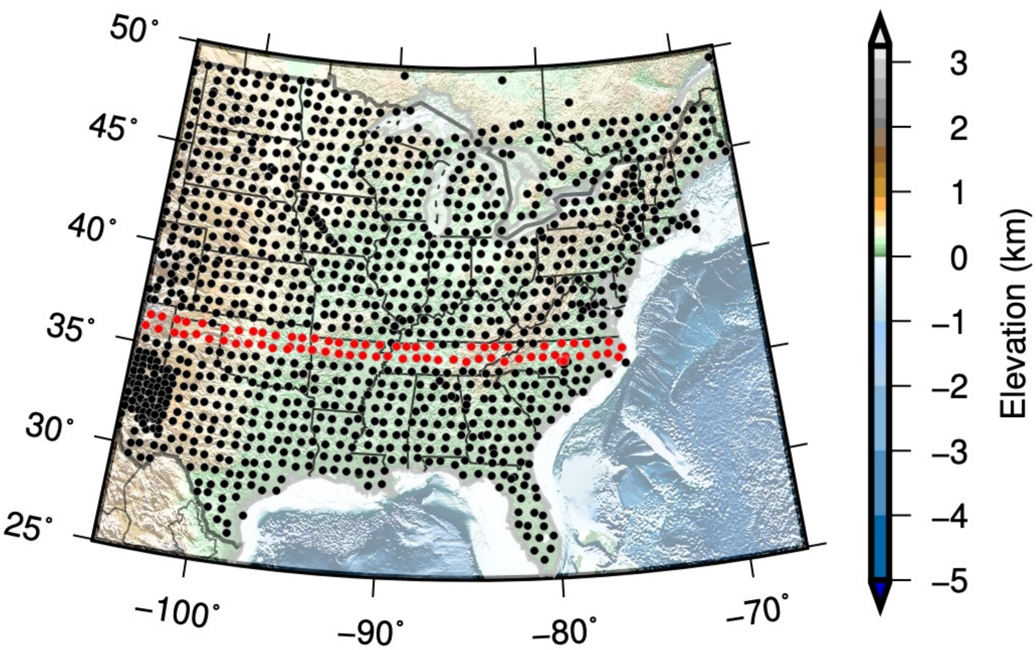

Figure S1. Map of the study region and seismic stations (dots) used in the receiver function wavefield smoothing/interpolation. Red dots show the stations used in Figure S6.

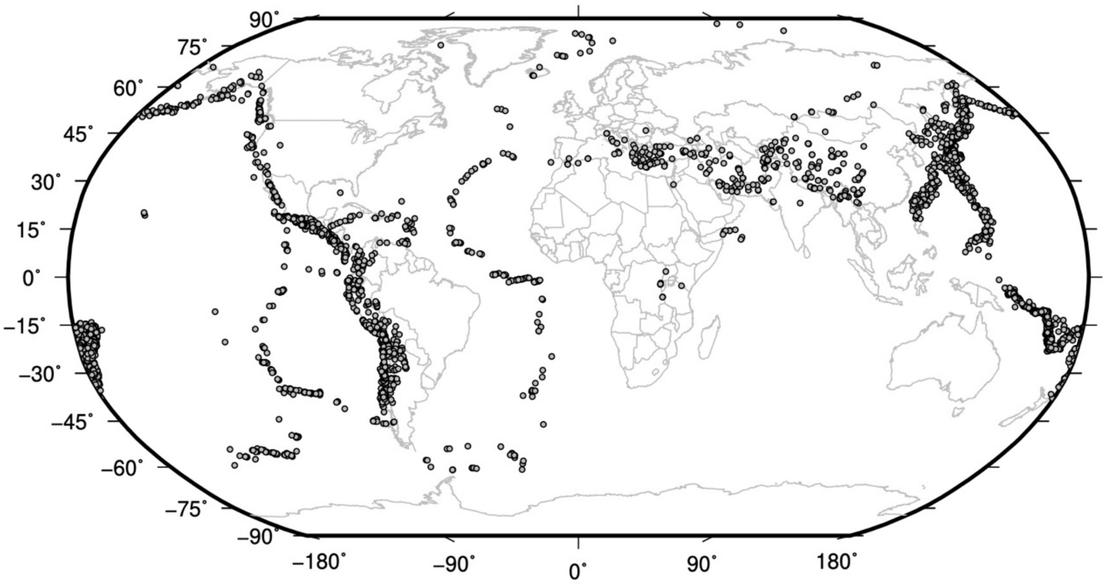

Figure S2. Seismic events (dots) used for the receiver function calculations.

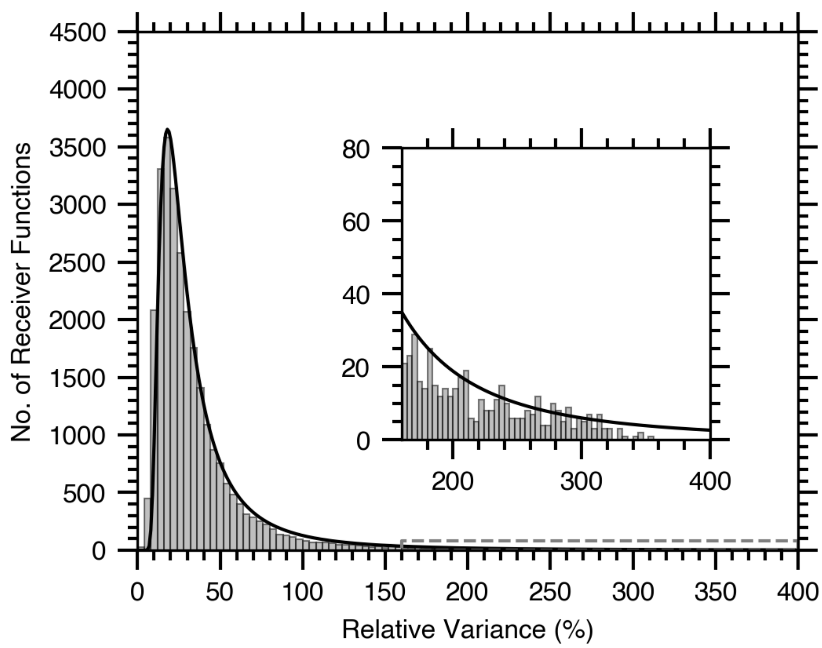

Figure S3. Relative data variance distribution of receiver functions recorded in the Eastern U.S. region. The insets show a detailed view for relative variance ranges between 165% and 400% (dashed box). Black lines indicate extreme value distributions. The relative data variance is computed as the signal variance between an individual receiver function and the single-station-averaged receiver function.

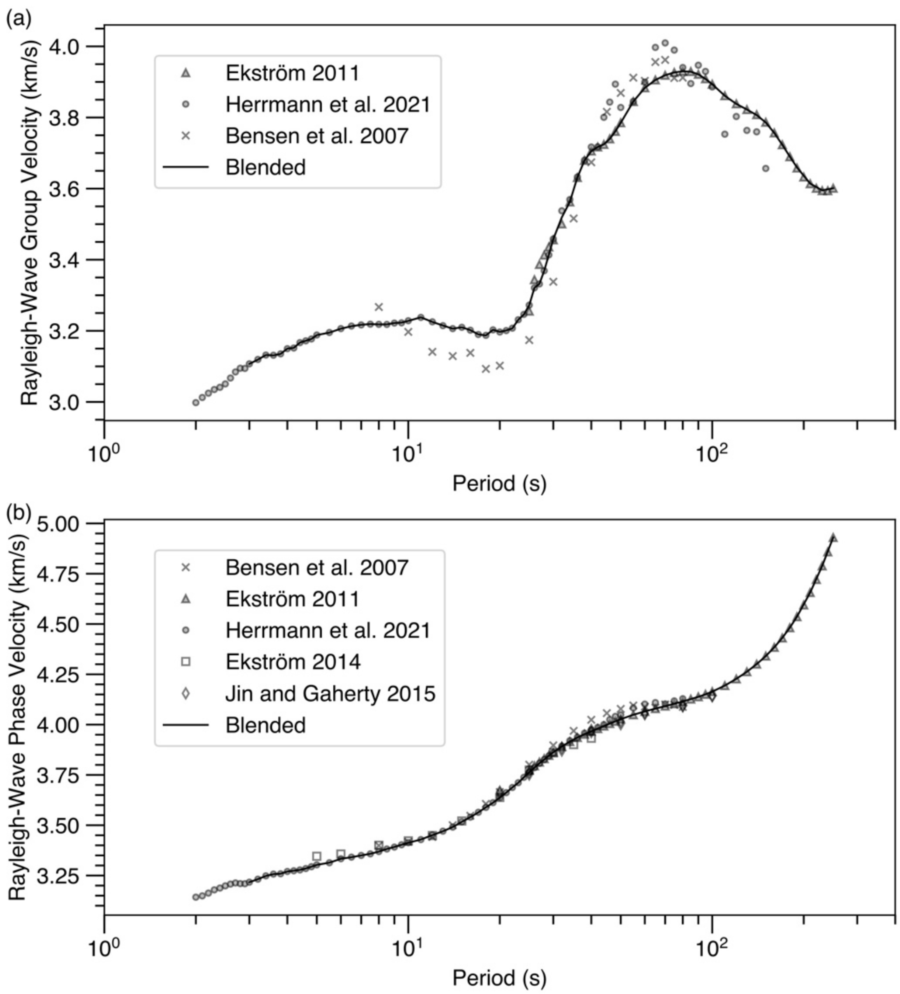

Figure S4. Example dispersion measurements and blended curves in the eastern U.S. (latitude 44.5˚N, longitude 73.5˚E) for (a) Rayleigh-Wave group velocity and (b) Rayleigh-Wave phase velocity. The blended curves were computed using values from Ekström (2011) and Herrmann et al. (2021). Dispersion models from other sources (Bensen et al., 2007; Ekström, 2014; Jin & Gaherty, 2015) are only shown for reference.

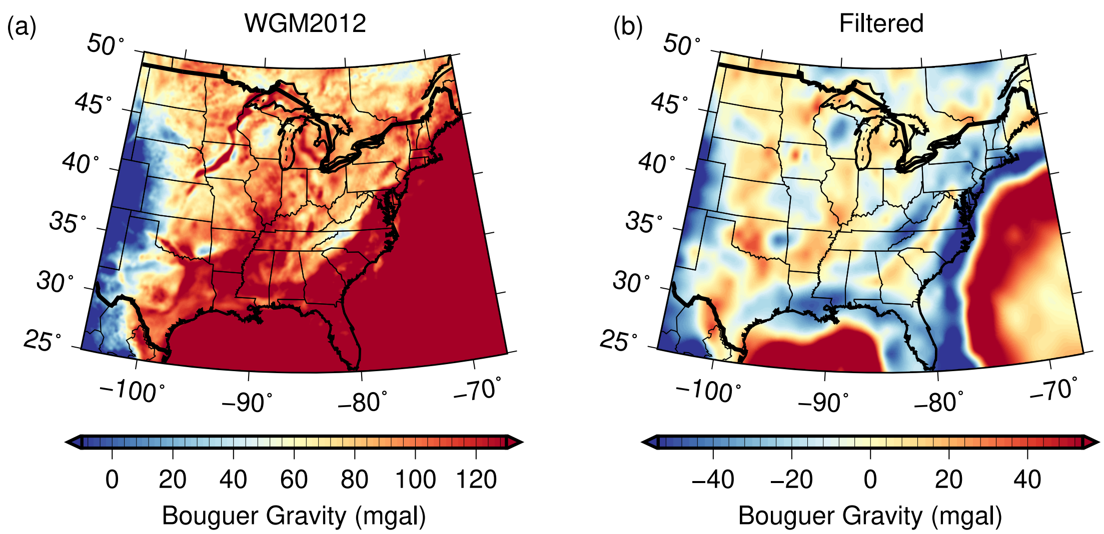

Figure S5. Bouguer gravity maps before (a) and after (b) wavenumber-filtering to emphasize gravity anomalies related to shallow structure and features have spatial dimension larger than 1˚. Note the color scale changes.

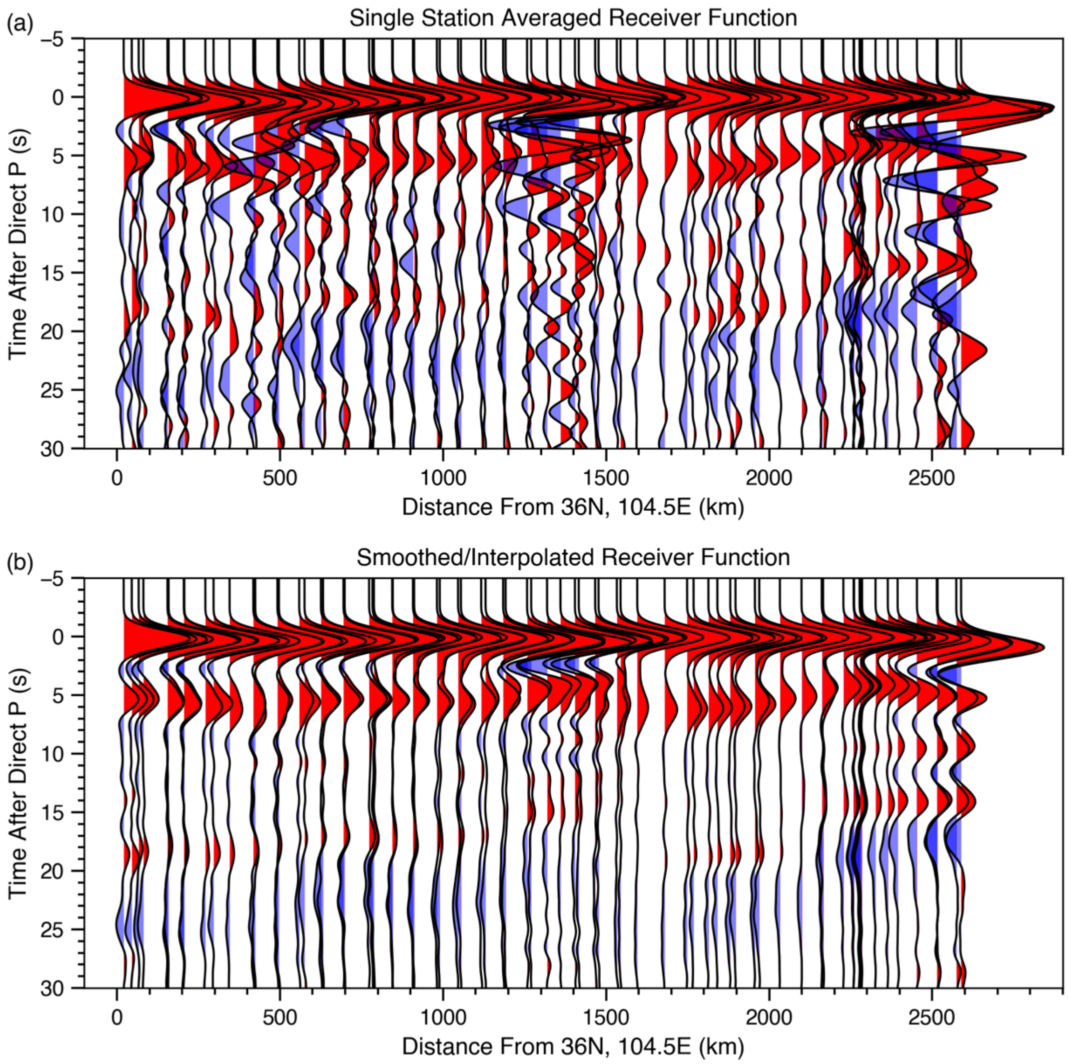

Figure S6. A comparison of (a) single station averaged and (b) smoothed/interpolated receiver functions in a cross-section view. The locations of the stations used are shown in Figure S1.

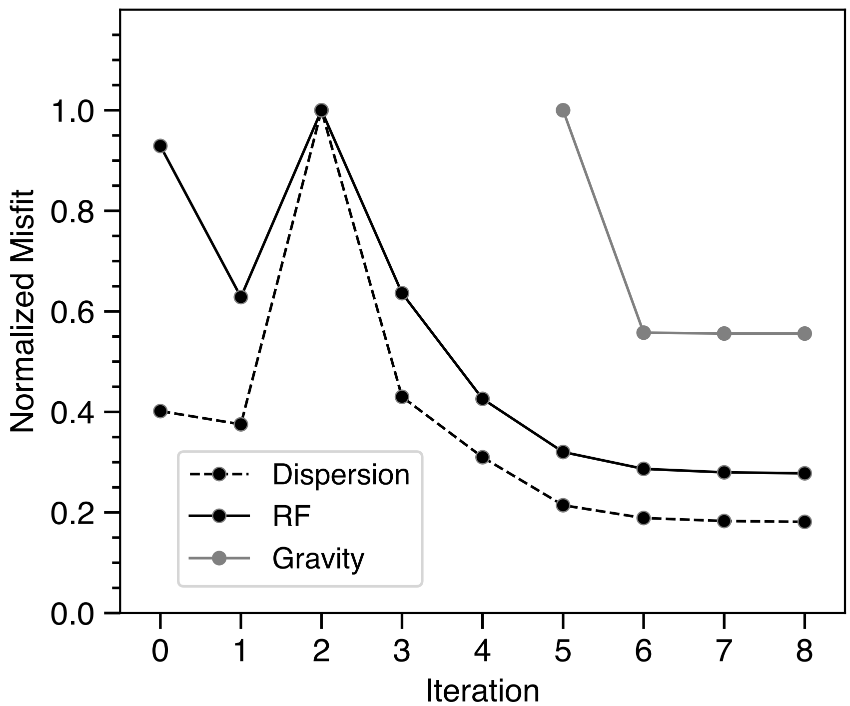

Figure S7. Convergence of the simultaneous inversion. The gravity observations were included in the last three iterations. Misfits for each type of observations are normalized with the maximum. For each iteration, misfits were averaged over the entire grid. At each grid location, dispersion misfit was averaged between group and phase velocity measurements while receiver function misfit was averaged from all available receiver functions. RF stands for receiver function.

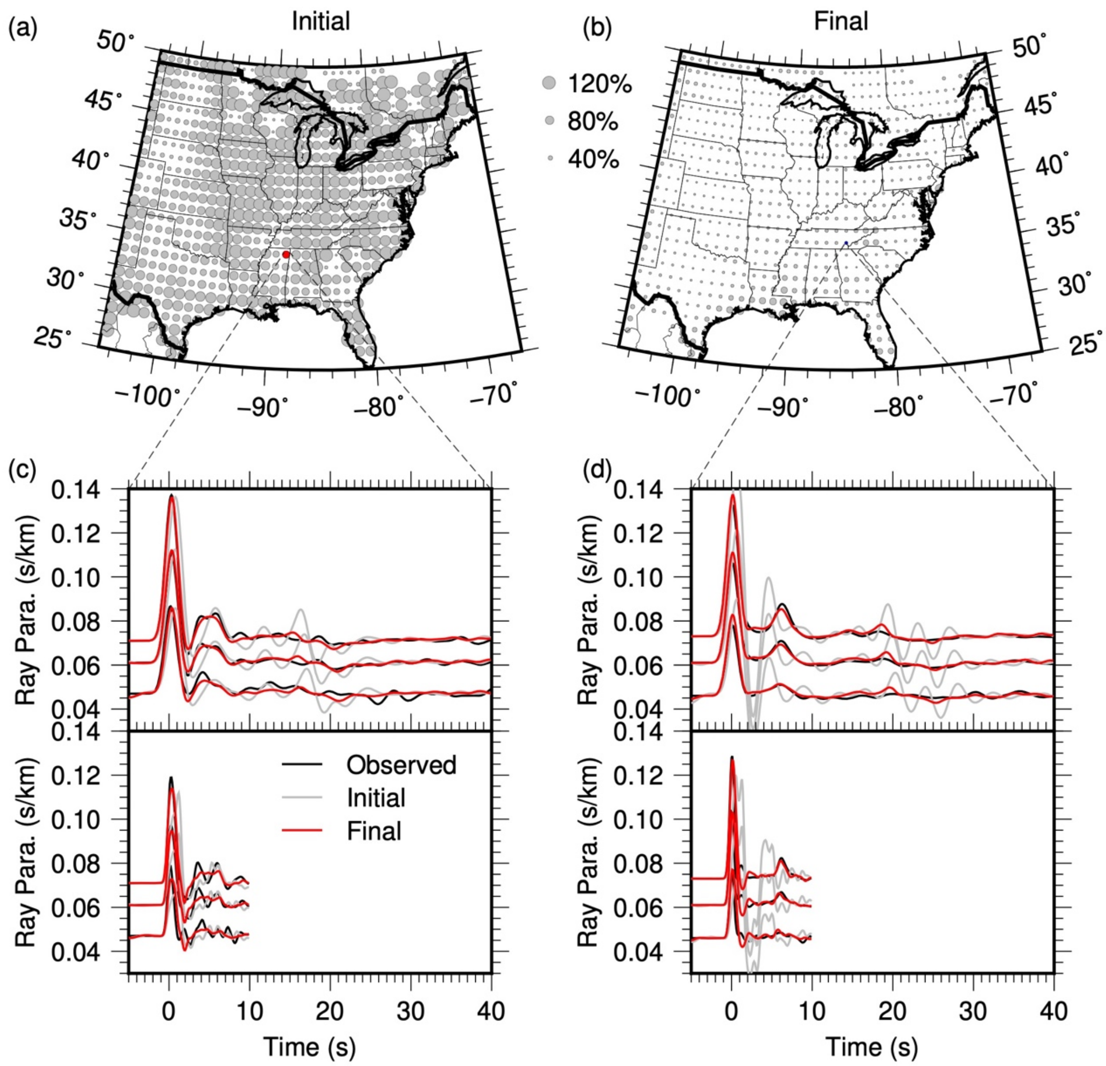

Figure S8. Maps showing the spatial distribution of receiver-function misfits for (a) the initial model and (b) the final model. The size of dots represents the normalized misfit at each grid point. Receiver functions at two grid points, (34.5˚, -88.5˚) and (35.5˚, -84.5˚), are showing in (c) and (d) with the locations indicated by the dashed black lines. Receiver functions with different ray parameters are displayed for both the narrow-band (Gaussian 1.0, top frame) and the broad-band (Gaussian 2.5, bottom frame). Since the broad-band receiver functions are noisier, we used a shorter time window.

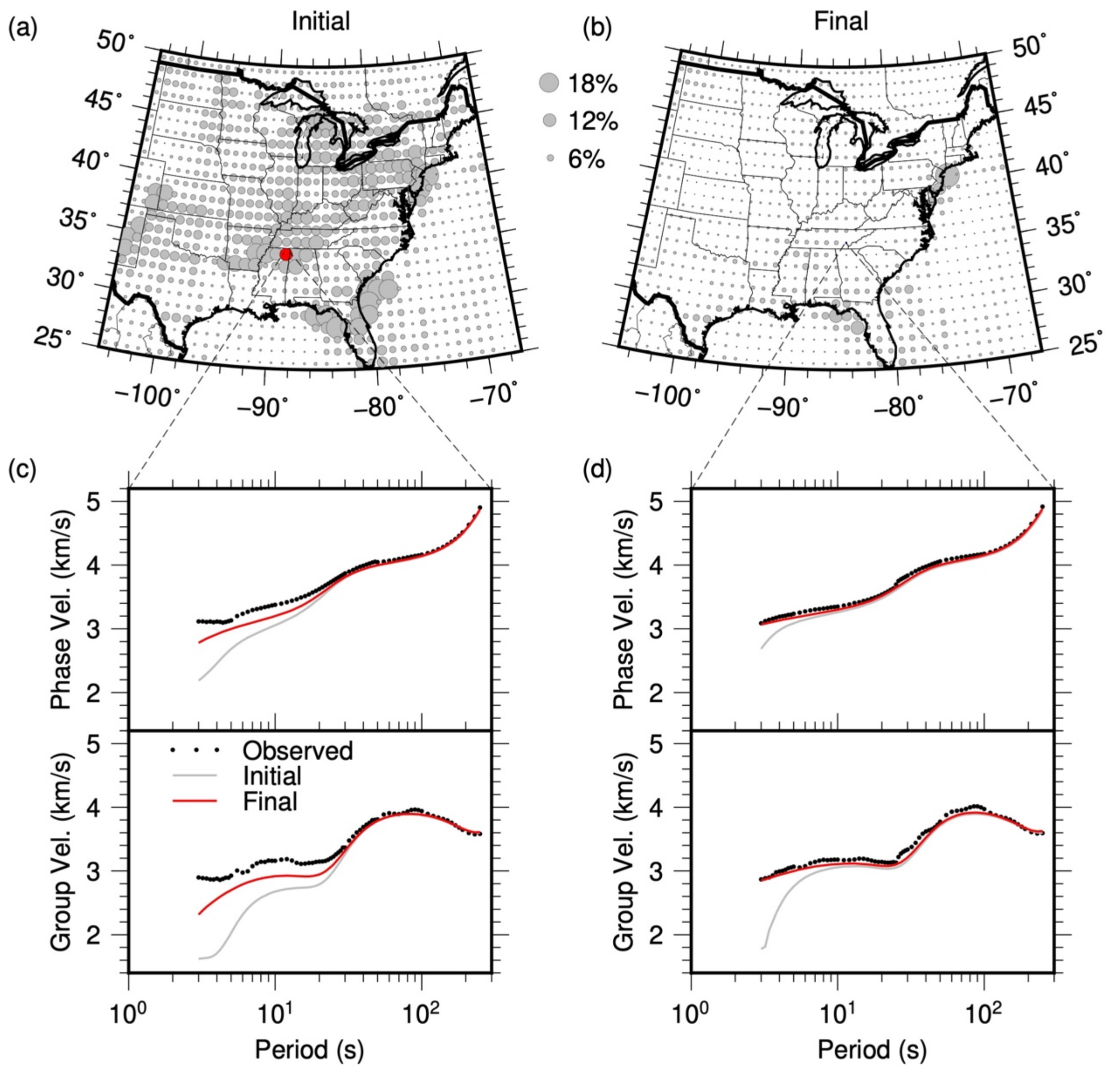

Figure S9. Maps showing the spatial distribution of the surface-wave dispersion misfits for (a) the initial model and (b) the inverted model. The size of dots represents normalized misfit at each grid points. Rayleigh-wave dispersion curves at two grid points, (34.5˚, -88.5˚) and (35.5˚, -84.5˚), are shown in (c) and (d) with the location indicated by the dashed black lines. The upper panel of (c) and (d) shows phase velocities while the lower panel shows group velocities.

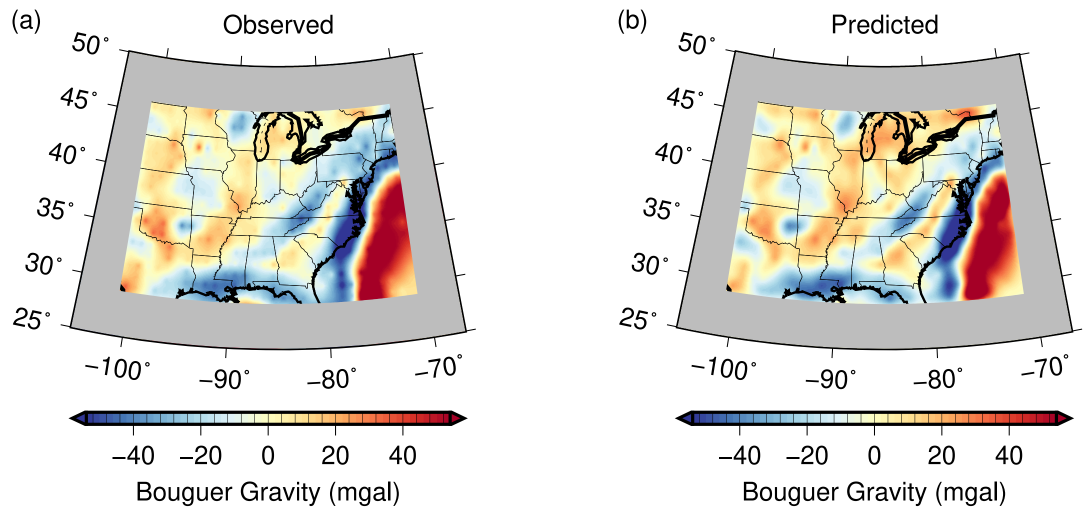

Figure S10. A comparison of (a) the observed gravity against (b) the predicted gravity for the eastern U.S.

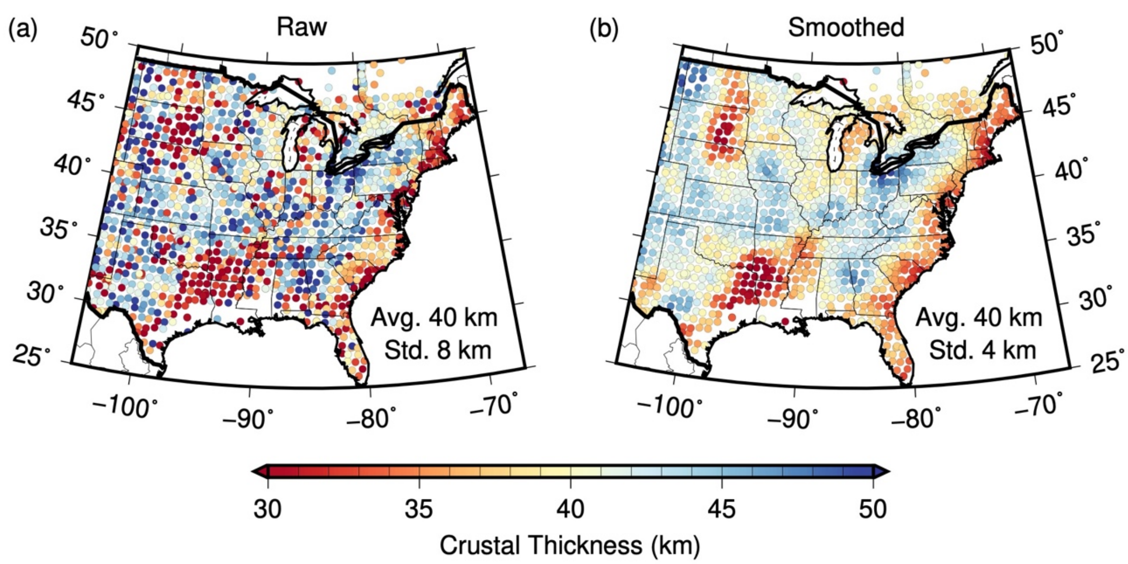

Figure S11. A comparison of EARS crustal thickness results (Crotwell & Owens, 2005) from (a) the raw data and (b) the spatially smoothed version.

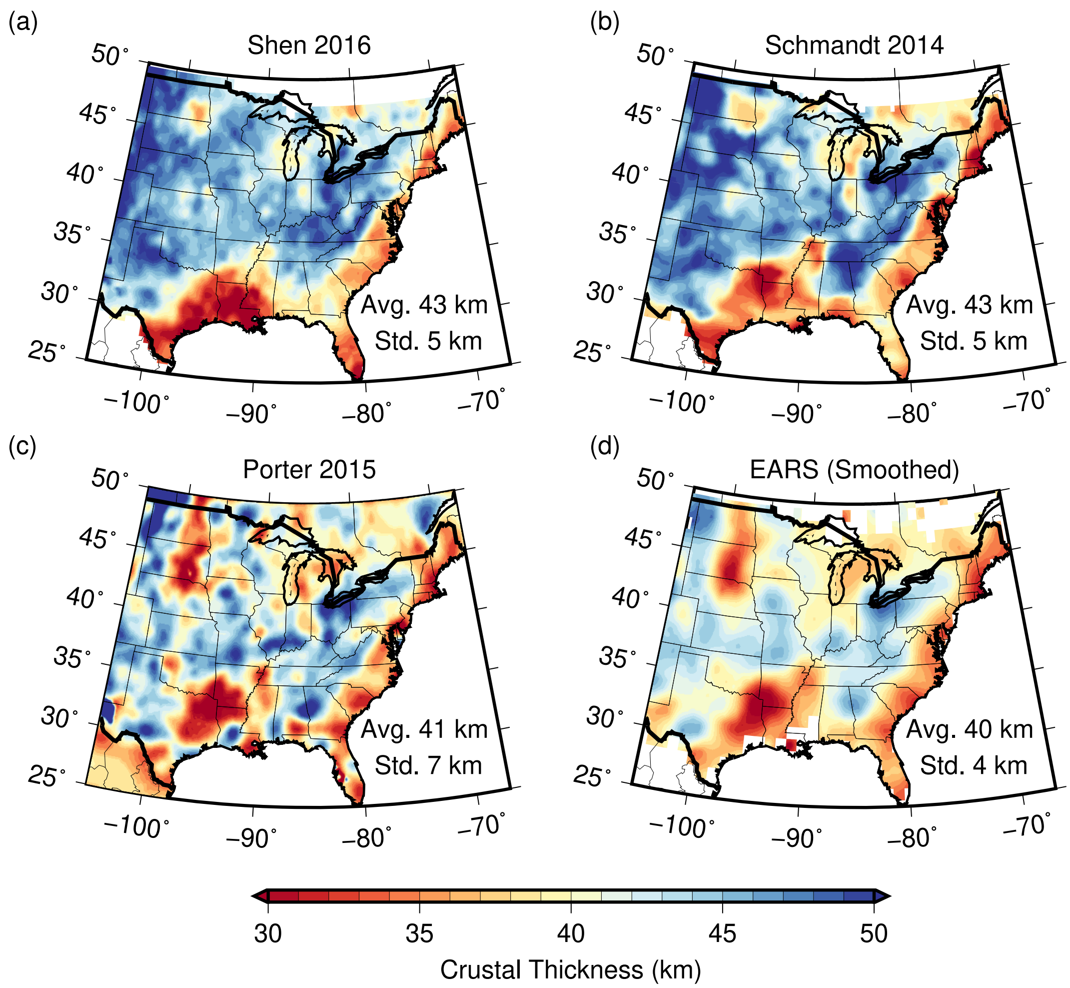

Figure S12. A comparison of crustal thickness maps from four recent models, (a) Shen-2016 model (Shen et al., 2016), (b) Schmandt-2014 model (Schmandt et al., 2015), (c) Porter-2015 model (Porter et al., 2016), and (d) the smoothed EARS model (Crotwell & Owens, 2005). The results of this paper are shown in Figure 5.

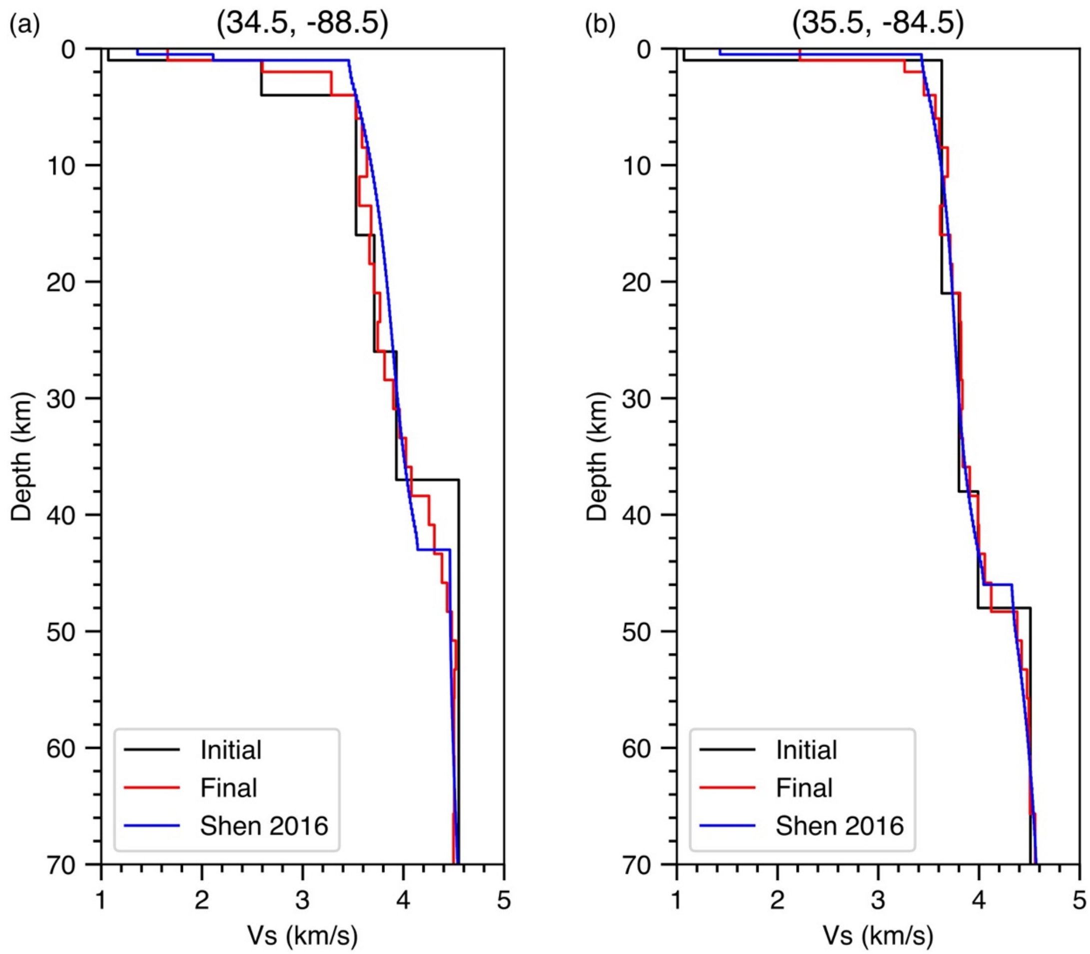

Figure S13. A comparison of 1D shear-wave velocity profiles at two grid points. The Shen-2016 model is extracted from Shen et al. (2016). The initial model is obtained from Crust 1.0. Correspoinding receiver functions and surface-wave dispersions can be found in Figure S8 and S9, respectively.

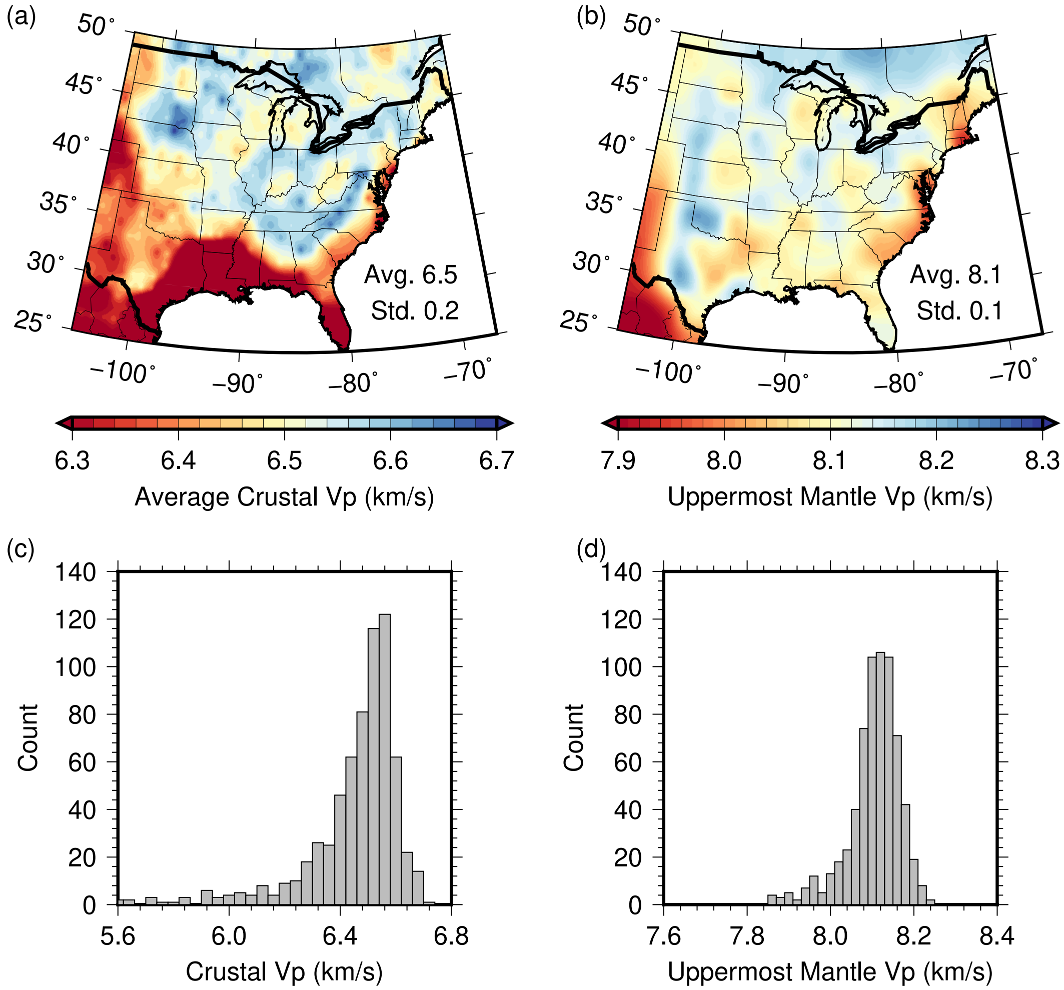

Figure S14. Maps showing (a) the averaged crustal V_p velocities, (b) uppermost mantle Vp velocities and histograms of (c) crustal and (d) uppermost mantle V_p velocity.

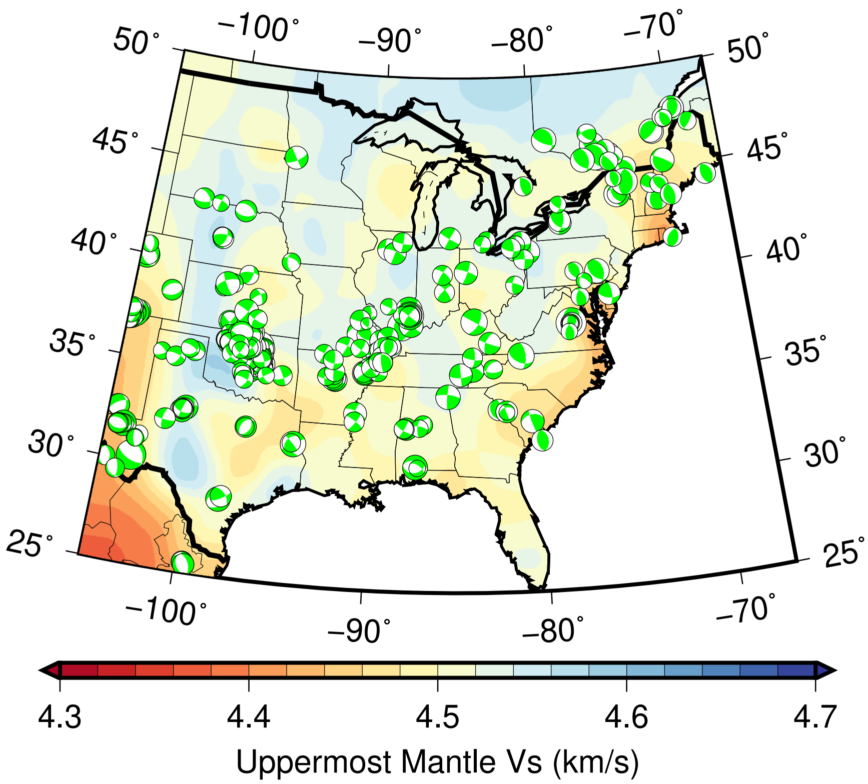

Figure S15. A comparison of the uppermost mantle V_s and focal mechanisms from the Saint Louis University (SLU) catalog (prior 2021/05/01).

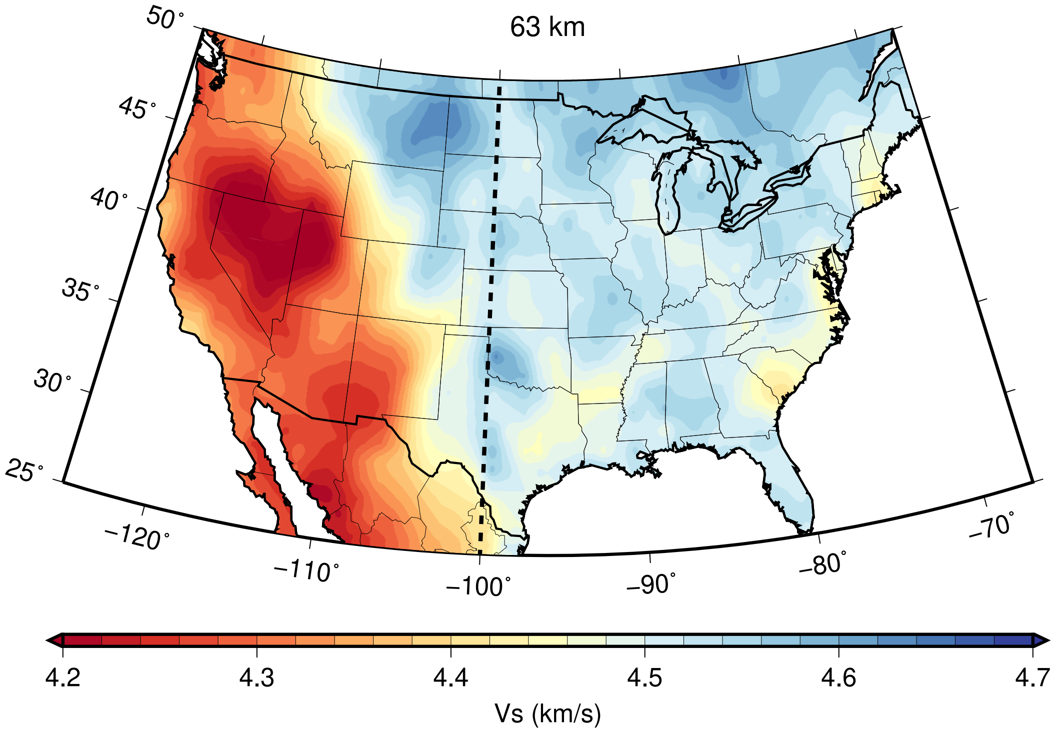

Figure S16. A comparison of the upper mantle shear speed at 63 km in western and eastern U.S. The dashed line indicates the transition from the western U.S. model (Chai et al., 2015) to the eastern U.S. model (this study).

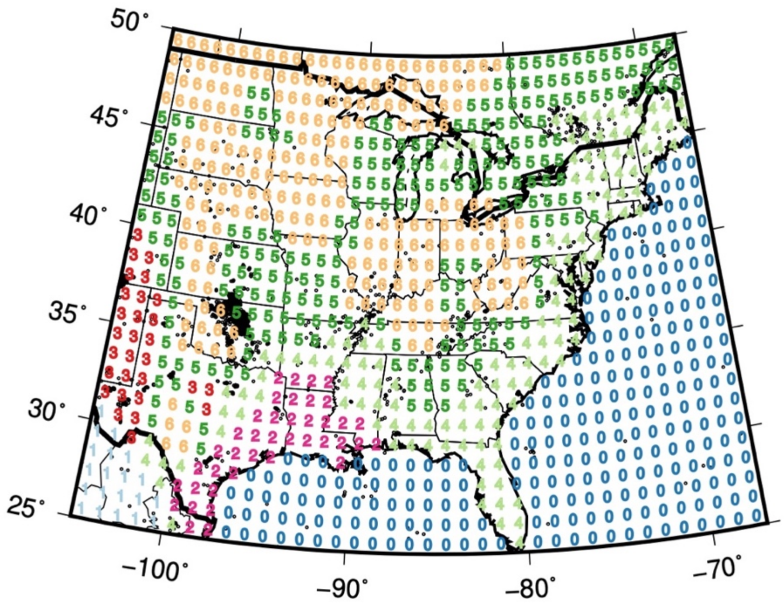

Figure S17. Spatial distributions of the automated model clusters generated using a simple hierarchical clustering algorithm. Similar 1D velocity profiles were grouped together as one cluster. Velocity profiles with large differences were assigned to different clusters. Each 1D velocity profile consists of shear velocities between 6 km and 200 km in depth. Note the oceanic profiles were assigned based on geographic location. The rough correspondence of the clusters to geologic regions are (0) Oceanic; (1) Southern Basin and Range Region; (2) Western Mississippi Embayment; (3) Central Basin and Range Region; (4) Atlantic Plain and Northern Appalachian Highlands; (5) and (6) Interior Plains, Central and Southern Appalachian Highlands, and Southern Canadian Shield. The velocity profiles within each cluster are summarized in Figure S18. Cirlces represent seismic events with a magnitude larger than 3 from the USGS NEIC catalog before May 2021.

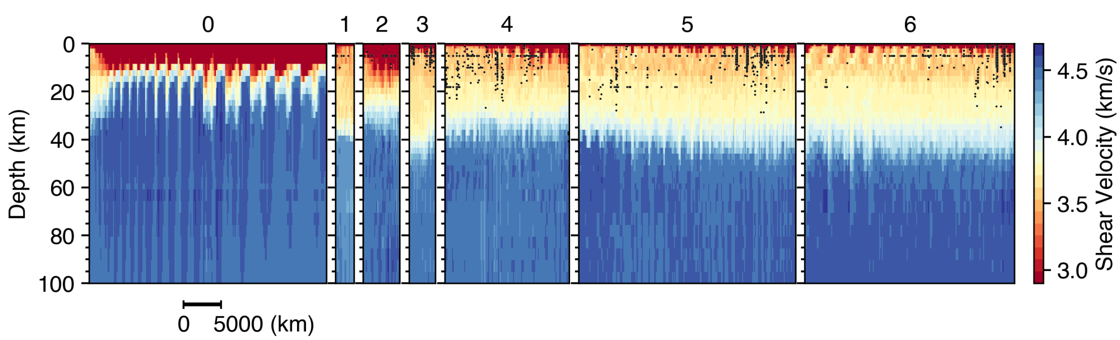

Figure S18. Shear velocity profiles of Earth model clusters corresponding to Figure S17. Each 1D velocity profile consists of shear velocities between 6 km and 200 km in depth. The label above each panel corresponds to a cluster in Figure S17. In each panel, individual 1D shear velocity profiles belong to the cluster are shown. Velocity profiles within the cluster are sorted from north to south by row (like in a book). Dots shows seismicity (magnitude 3 and larger) from the USGS NEIC catalog before May 2021.

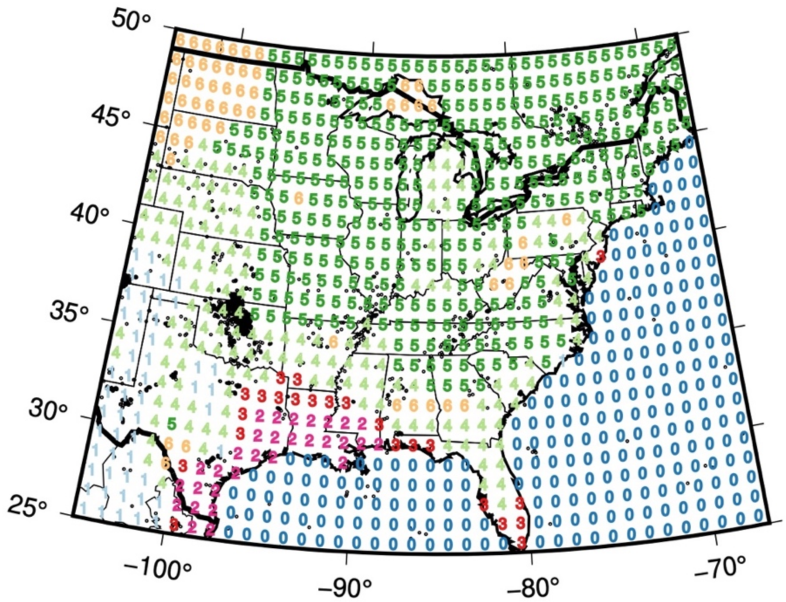

Figure S19. Same as Figure S17 but used the shear velocities of the upper 20 km.

.

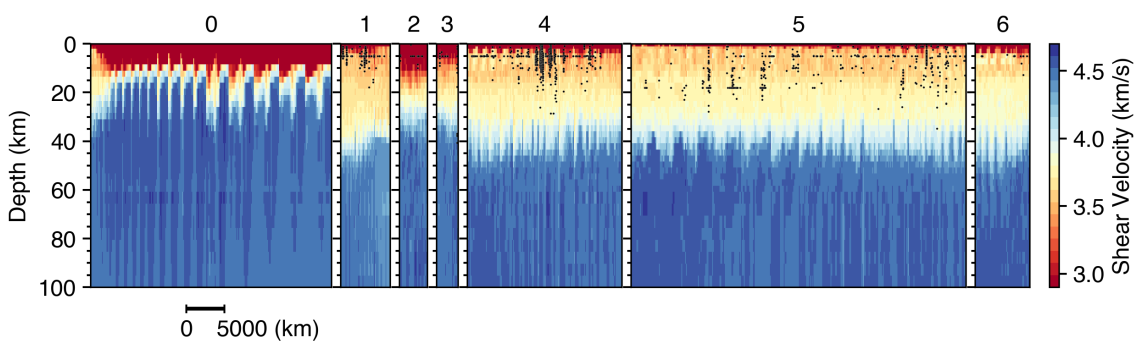

Figure S20. Same as Figure S18 but the clustering used the shear velocities of the upper 20 km. The label above each panel correspond to that in Figure S19.

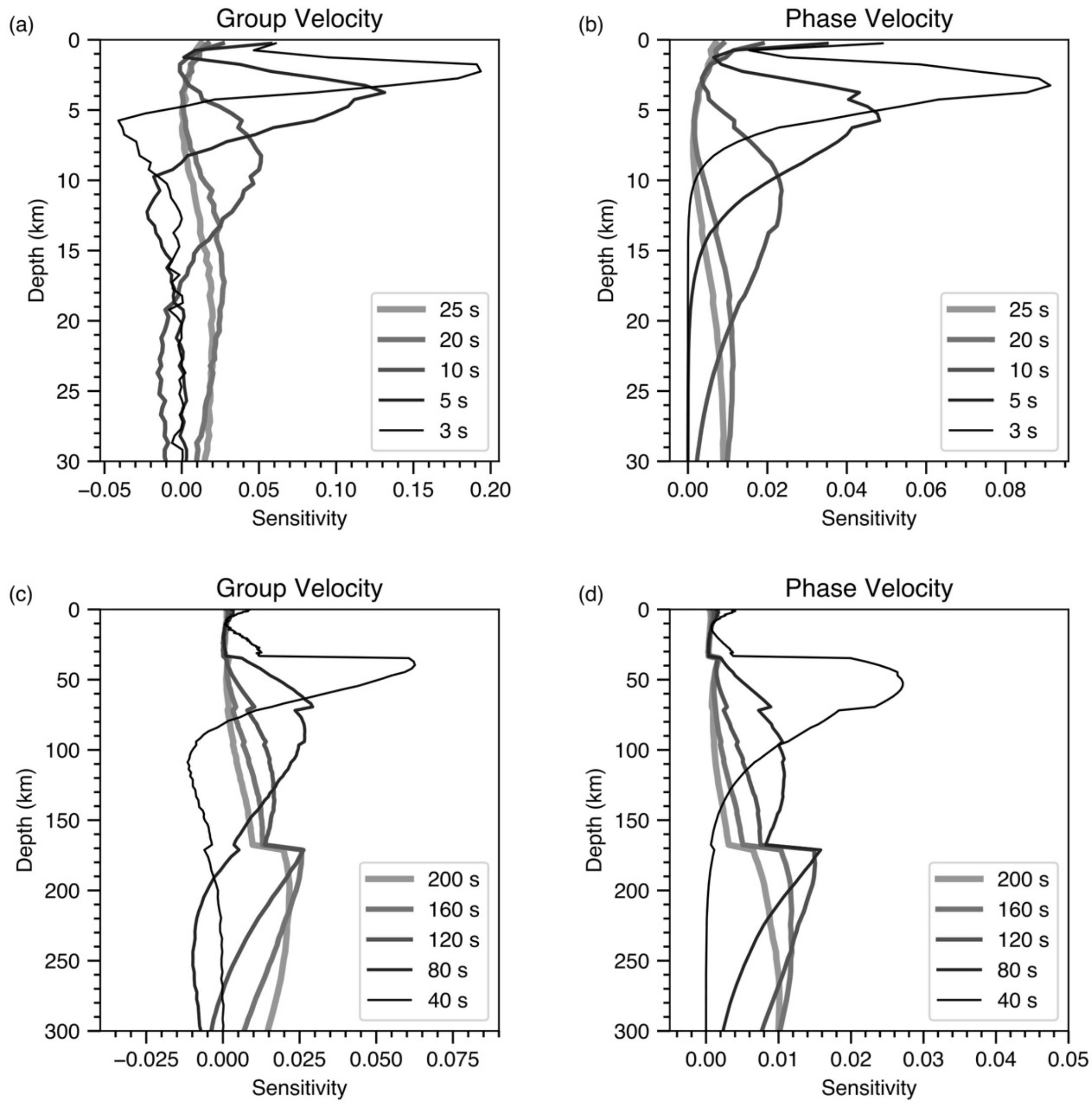

Figure S21. Rayleigh wave sensitivity to shear wave velocity.

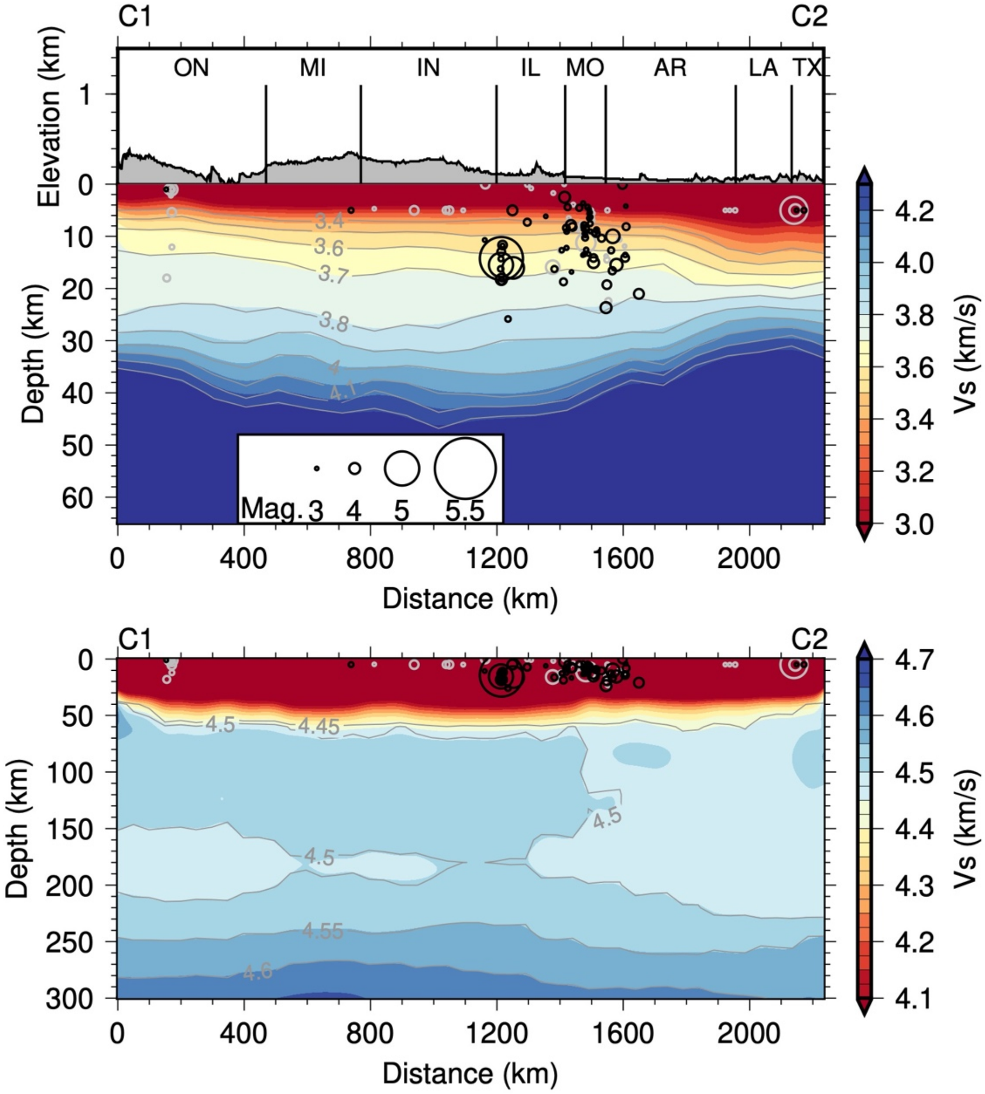

Figure S22. Shear velocity cross-sections along C1-C2. Top panel used a color palette that is suitable for crustal speeds. The lower panel shows shear-wave velocity using a color palette more suitable for mantle speeds. Circles are earthquakes located within 100 km of the cross-section. Black circles are events with depth uncertainties less than 5 km. Gray circles represent earthquakes with larger depth uncertainties or without uncertainties. Note the image is vertically exaggerated.

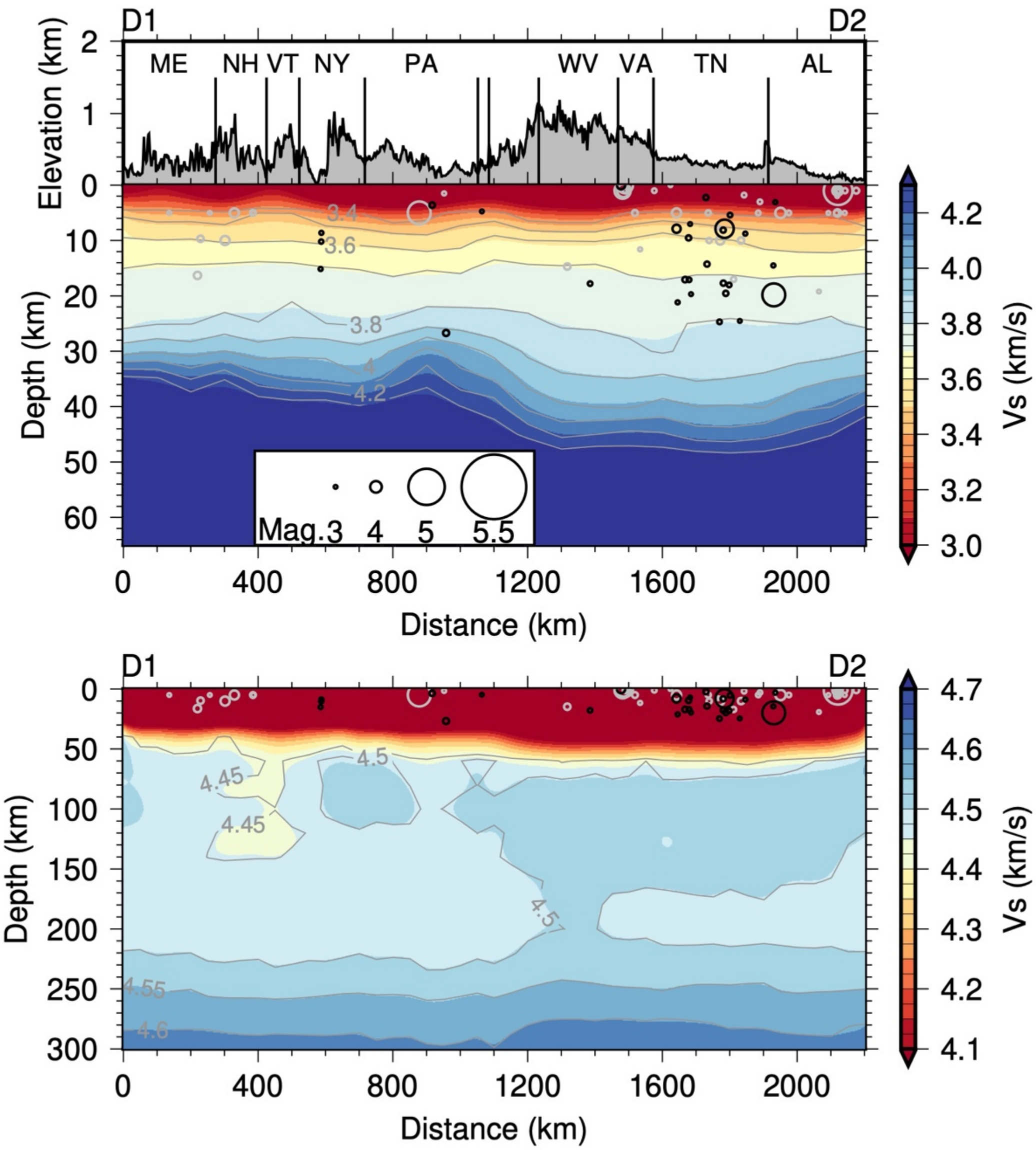

Figure S23. Same as Figure S22 but for cross-section D1-D2.

260 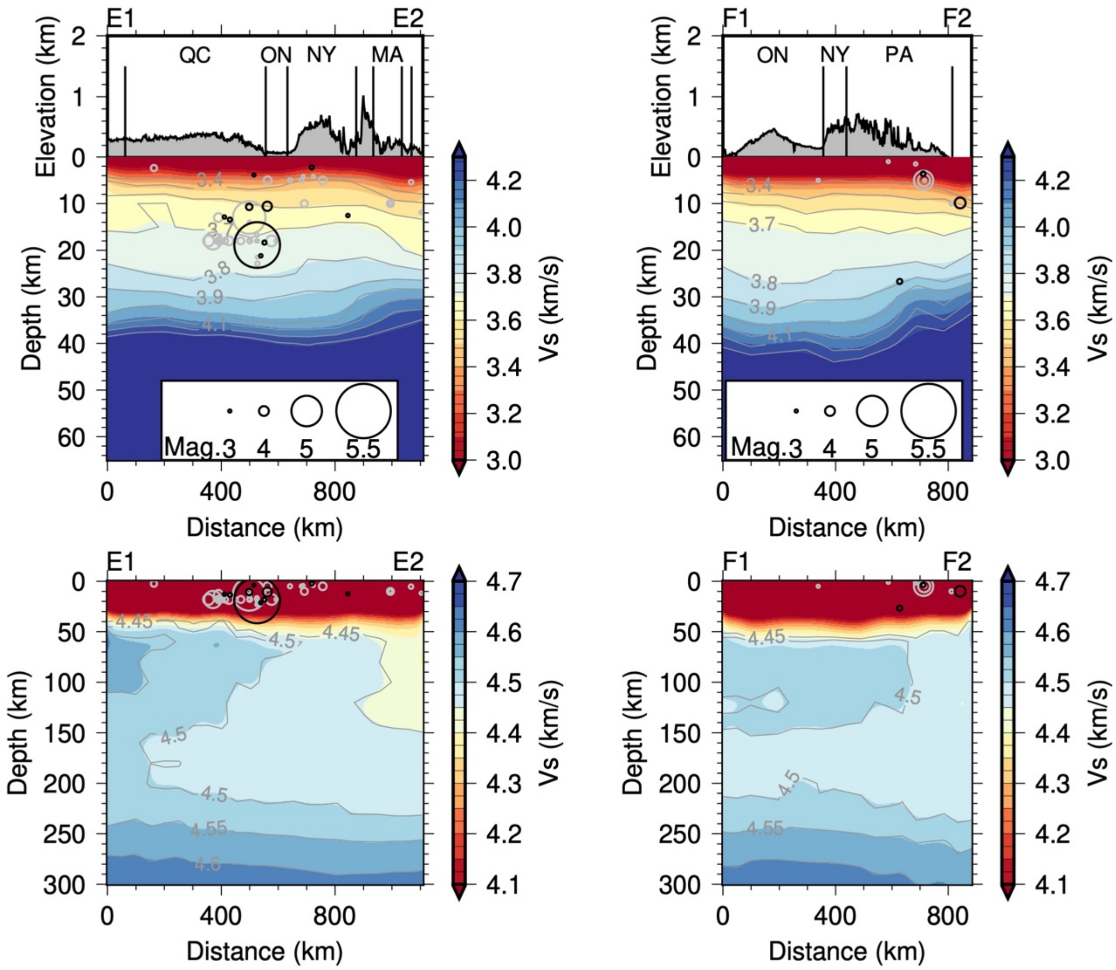

261 **Figure S24.** Same as Figure S22 but for cross-sections E1-E2 and F1-F2.

262

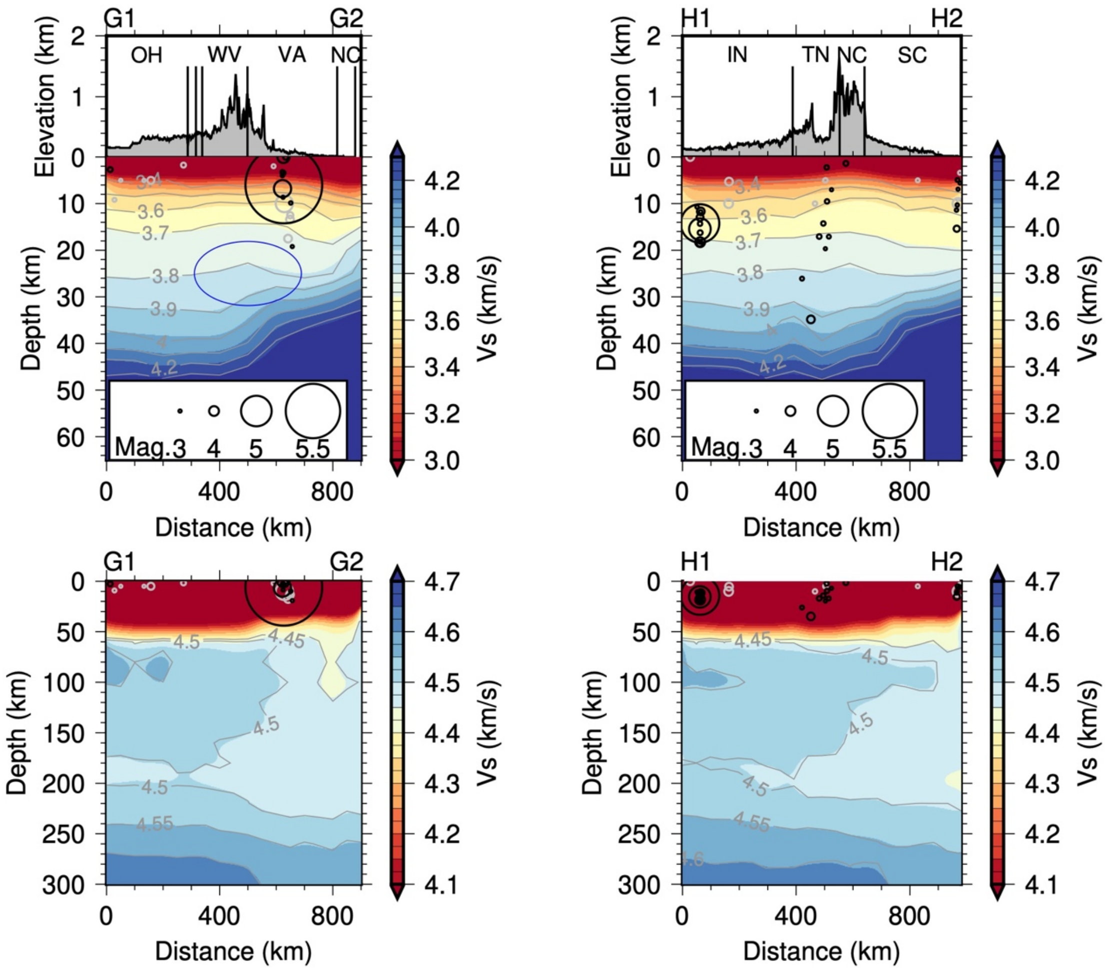

Figure S25. Same as Figure S22 but for cross-section G1-G2 and H1-H2. The solid ellipse incidates a faster lower curst anomaly.

Table S1. A list of seismic networks used for the receiver function calculation.

Data Set S1. The final seismic velocity model for the eastern United States derived from the inversion. The first column is latitude. The second column is longitude. The third column is depth (top of the cell) in kilometers. The fourth, fifth and sixth column are P-wave velocity (km/s), S-wave velocity (km/s), and density (g/cm^3), respectively.

Data Set S2. The seismic velocity model for the western United States from Chai et al. (2015). The first column is latitude. The second column is longitude. The third column is depth (top of the cell) in kilometers. The fourth, fifth and sixth column are P-wave velocity (km/s), S-wave velocity (km/s), and density (g/cm^3), respectively.

Movie S1. An animation compares the single-station-averaged receiver functions against the spatially smoothed/interpolated receiver functions.

Visualization S1. An interactive tool to view S-wave velocities of the 3D model for the eastern United States as depth slides and depth profiles side by side. The visualization was created with a Python script developed by Chai et al. (2018).

Visualization S2. An interactive tool to view S-wave velocities of the 3D model for the western United States (from Chai et al., 2015) as depth slides and depth profiles side by side. The visualization was created with a Python script developed by Chai et al. (2018).